Simulations of shade tolerant solar cells with low breakdown voltages

B. Huang

TU Delft

PVMD
Delft University of Technology

Simulations of shade tolerant solar cells with low breakdown voltages

by

B. Huang

in partial fulfillment of the requirements for Master of Science
Sustainable Energy Technology
at the Delft University of Technology,
to be defended publicly on Wednesday July 14, 2021 at 10:00 AM.

Student number:	5047978	
Project duration:	November 16, 2020 – July 14, 2021	
Supervisors:	Msc. Andres Calcabrini,	daily supervisor
	Dr. Paul Procel Moya,	supervisor
	Dr. Patrizio Manganiello	supervisor
Thesis committee:	Dr. Olindo Isabella,	PVMD/ESE, TU Delft
	Dr. Patrizio Manganiello,	PVMD/ESE, TU Delft
	Dr. Aditya Shekhar,	DC&S/ESE, TU Delft
	Dr. Paul Procel Moya,	external expert
	Msc. Andres Calcabrini	PVMD/ESE, TU Delft

This thesis is confidential and cannot be made public until July 14, 2023.

An electronic version of this thesis is available at `http://repository.tudelft.nl/`.

TU Delft

Abstract

Shading on photovoltaic modules is practically inevitable, especially in urban environments. The shadows cast by neighbouring objects on the solar panel force shaded solar cells to operate under reverse bias. In this case, instead of generating power, the shaded solar cell dissipates power, which is converted into heat and may induce the formation of hot-spots. Many attempts have been made to improve the shade tolerance photovoltaic modules. In this work, we focus on solar cells with low breakdown characteristics to build shade tolerant photovoltaic modules. These types of solar cells allow the current flow at low reverse bias voltages (around $-4\,\mathrm{V}$). The main design challenge is to maintain high conversion efficiencies while achieving low breakdown voltages.

In order to design shade tolerant photovoltaic modules, the carrier transport mechanisms in the solar cell under reverse bias conditions are firstly investigated. A robust simulation template is created in Sentaurus TCAD to perform a parametric evaluation, including both the structural and operating parameters, of the device I-V characteristics. The silicon heterojunction interdigitated back contact solar cell with a silicon oxide passivation layer is among the most promising cell structures to achieve both the low breakdown voltage and the high efficiency. Band-to-band tunneling happens between the heavily doped p^+ and n^+ regions at the rear side, which allow charge carriers to recombine without entering the bulk of the solar cell. We analyse the effect of the tunneling mass, the gap distance and the dopants penetration length on the forward and reverse I-V curves. Simulations suggest that it is possible to design high efficiency solar cells with breakdown voltages as low as $-1.2\,\mathrm{V}$. In addition, device performances under different temperature and irradiance conditions are analysed for the purpose of further investigations on the system level.

While this research study is mainly focused on the performance of solar cells, the results presented in this thesis facilitate comprehensive system level energy yield analyses of shade tolerant photovoltaic modules with low breakdown voltage solar cells.

Acknowledgements

With this master thesis, I am about to end my studies at Delft University of Technology after two amazing years. The rigorous academic training deepens my knowledge in this field and the well organized clusters encourage me to keep making contributions towards a renewable future. The life here in Delft will always be a precious experience in my life.

During this unusual period, I am really grateful to Andres Calcabrini, Dr. P. A. Procel Moya and Dr. Patrizio Manganiello for doing my master thesis under their supervisions in PVMD group. Their encouragements and support are of vital importance to me for accomplishing my thesis project.

I would like to thank my daily supervisor Andres first for continuously motivating and inspiring me to gain as much knowledge as possible, and Andres deserves the best daily supervisor award. My thesis aims to bridge the gap between cell designs and solar system operations while Andres managed to bridge the gap between me in November and my thesis objectives. I would also like to thank Dr. P.A. Procel Moya for his strong support and great insights in both simulations and fundamental physics whenever I was in trouble. I am really grateful to Dr. Patrizio Manganiello for his guidance during the entire thesis project. It was Dr. Manganiello who brought me to this topic and kept me making progress during those precious discussions. I did enjoy the whole journey with my supervisors. I would like to thank Dr. Olindo Isabella and Dr. Aditya Shekhar for being part of my graduation committee.

Thanks to all the friends during these two years. Thanks to the best teammates Jose, Zhi, Daniela, Andya, Jing for our excellent teamwork. Thanks to Tim and Julian for generous help in technical writing. Thanks to Chaofeng for our discussions about cell technologies during cycling in almost every weekend. Thanks to Lambor and Echo for our countless memories and happiness in Germany and Italy.

My thanks also go to my friends, Vivien, Frank, Colin, Diana and so on, since primary school. The lock-down in April and November last year were suffering. Depression came to everyone but fortunately we were together to overcome all the obstacles. I really missed the online game and chat parties back then.

Finally, my sincere gratitude to my family for their unconditional support and love during these two years in the Netherlands.

Ben Huang
Delft, July 2021

Contents

Abstract iii

Acknowledgements v

1 Introduction 1
- 1.1 Solar energy . . . 1
- 1.2 Photovoltaic applications . . . 2
- 1.3 Partial shading and bypass diodes . . . 2
- 1.4 Problem statement . . . 5
- 1.5 Research goal and outline . . . 5

2 Fundamentals 7
- 2.1 Working principles of solar cells . . . 7
  - 2.1.1 Generation of charge carriers . . . 7
  - 2.1.2 Separation and collection of charge carriers . . . 8
- 2.2 Comprehensive complements of solar cells . . . 9
  - 2.2.1 Anti-reflection coating . . . 9
  - 2.2.2 Passivations . . . 10
  - 2.2.3 Transparent conductive oxides . . . 10
- 2.3 Breakdown mechanisms . . . 11
- 2.4 Front back contacted solar cells . . . 12
  - 2.4.1 Breakdown mechanisms in front back contacted solar cells . . . 13
  - 2.4.2 Temperature coefficient of breakdown mechanisms in front back contacted solar cells . . . 14
- 2.5 Interdigitated back contact solar cells . . . 14
  - 2.5.1 Breakdown mechanisms in IBC solar cells . . . 15
  - 2.5.2 Temperature coefficients of breakdown mechanisms in IBC solar cells . . . 16
  - 2.5.3 Reverse characteristics of IBC solar panel . . . 16
- 2.6 IBC solar cells with low reverse characteristics . . . 17
  - 2.6.1 Maxeon solar cells . . . 17
  - 2.6.2 IBC-SHJ POLO solar cells . . . 18
  - 2.6.3 Homojunction IBC solar cells . . . 18
  - 2.6.4 Soft breakdown IBC solar cells . . . 19
- 2.7 Reflections . . . 19

3 Device Simulation 21
- 3.1 Simulations of solar cells in Sentaurus TCAD . . . 21
- 3.2 Generation of geometric structures in Sentaurus structure editor . . . 21
- 3.3 Physics in Sentaurus device . . . 22
  - 3.3.1 The poisson equation and quasi Fermi levels . . . 22
  - 3.3.2 Carrier transport in semiconductors . . . 24
  - 3.3.3 Carrier mobility . . . 24
  - 3.3.4 Band structure of semiconductors . . . 25
  - 3.3.5 Generation and recombination processes . . . 25
  - 3.3.6 Band-to-band tunneling . . . 26
- 3.4 External circuit connections in Sentaurus . . . 27
- 3.5 Reflections . . . 27

4 Simulations of structural parameters 29
4.1 Gap region between the emitter and the BSF . . . 29
4.2 Tunneling between the emitter and the BSF. . . . 30
4.3 Effect of the tunneling mass. . . . 31
4.4 Effect of the gap distance . . . 32
4.5 Effect of the dopant diffusion length . . . 33
4.5.1 Dopant concentration within the gap region. . . . 33
4.5.2 Electric I-V characteristics . . . 34
4.6 Reflections . . . 35

5 Effect of working conditions parameters 37
5.1 Irradiance simulation . . . 37
5.1.1 Absorbed photon density . . . 37
5.1.2 Effect on the breakdown voltage . . . 38
5.2 Thermal simulations . . . 40
5.2.1 Device temperature . . . 40
5.2.2 Effect on the breakdown voltage . . . 40
5.3 Reflections . . . 42

6 Conclusions and recommendations 43
6.1 Conclusions. . . . 43
6.2 Recommendations . . . 44

Bibliography 45

1 Introduction

1.1. Solar energy

The past 120 years have witnessed a rapid growth in world population, from 1.7 million to 6.9 million while the economic development has boosted significantly in the same time [1]. Both of the expansions are forcefully supported by the abundant energy supply. Figure 1.1 illustrates the growth of global energy supply, increasing by 1400% during the past centuries.

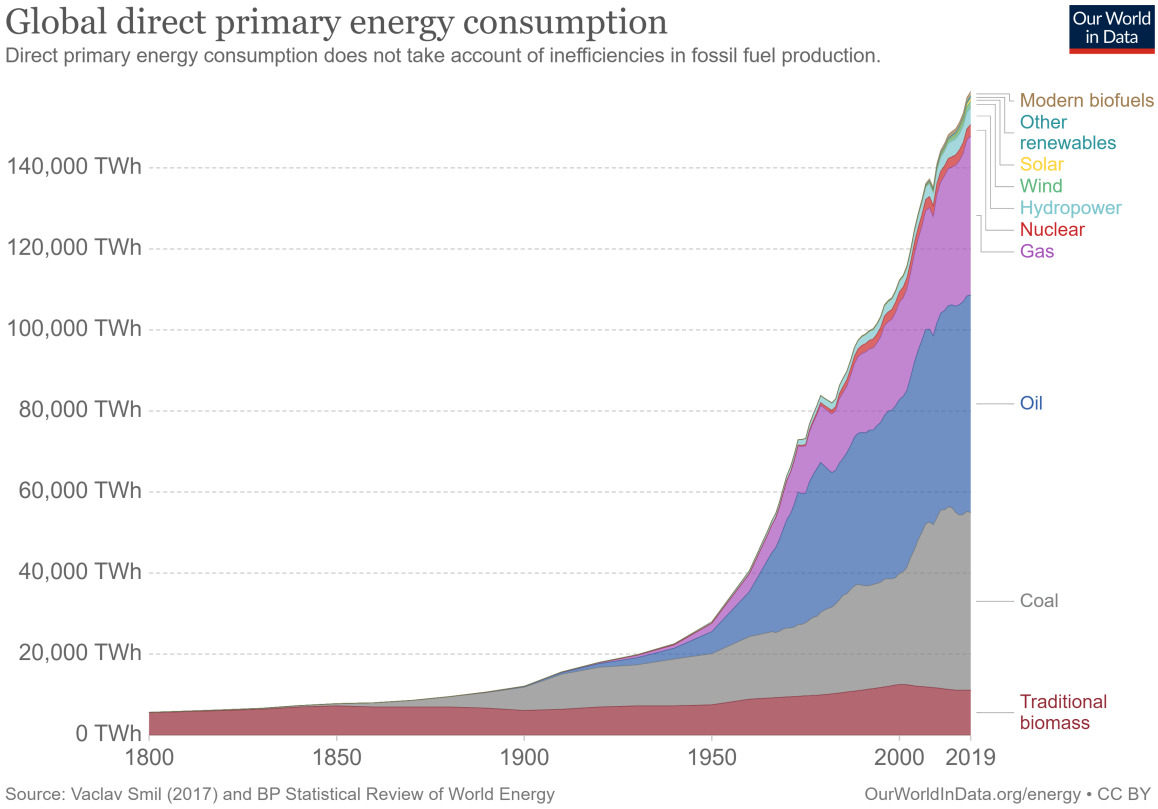

Figure 1.1: Global energy supply in sectors retrieved from [2]

The dominance of traditional fossil fuels in the existing power generation sector would raise series of environmental problems, including the immense emission of carbon dioxide, and would accelerate global warming effect [3]. Looking to the future, the anticipated world population in 2050 is estimated at 9.7 billion. In the meantime, the total global energy demand is supposed to rise at an even higher rate [4]. Therefore,

the Paris Agreement has been ratified and countries have scaled up renewable energy in order to capture the exponentially increasing energy demand and to sharply reduce the energy-related CO_2 emissions [5].

Since the Sun is the primary energy source for almost every process happening on Earth and the amount of solar energy incident on Earth is around 10,000 times larger than the total energy consumption of mankind within the same period [6], photovoltaic technology is believed to be the most promising energy generation method for harvesting solar energy directly and being utilized in decentralized ways.

1.2. Photovoltaic applications

Photovoltaic (PV) technology can be traced back to the year 1876 when the British natural philosopher William Grylls Adams demonstrated the photovoltaic effect on a platinum and selenium based junction with his student [6]. The generation of a potential difference at a junction consisted of two different materials is in response to the electromagnetic radiation [7]. Electrons are emitted from a material that absorbs light with an energy exceeding a threshold value. Based on that emerges devices like solar cells [8]. In 1954, three scientists Daryl M. Chapin, Calvin S. Fuller and Gerald L. Pearson made the first silicon-based solar cell with an efficiency of 6 % [6], and a heavy investment in the PV industry has occured since then.

A typical photovoltaic system employs several solar modules, each consisting a number of solar cells to generate electric power. There has been a boost in the photovoltaic installations in the past 50 years [9]. These PV installations could be adjusted according to different working conditions. Roof-mounted, wall-mounted, ground-mounted and even floating installations are implemented in various situations [10]. Due to its flexibility, PV systems have been utilized as the stand-alone power systems or the grid-connected ones. The production of the PV modules has been enormous since the 21st century when the Eurosolar organization started the ten thousand roof program with the government funding [11].

Nowadays, the global installed photovoltaic power capacity, from the simplest one-module-one-load system to the large power plants, has exceeded 1 GWp [9]. The majority of the installed capacity belongs to the solar power plants while the largest proportion of its growth lies in the residential sector. The ground-mounted installations are mostly for those large-scale power plants while there is considerable diversity in residential solar systems. Unlike those power plants, the landscapes of urban environment would lead to various operating conditions. The ever changing conditions would definitely influence the performance of these PV modules and the most prominent, among which, is the partial shading condition [12].

1.3. Partial shading and bypass diodes

Partial shading describes the condition of unevenly distributed irradiation on the solar modules. From a macro perspective, the annual energy yield of PV modules in urban environment is lower than that in solar power plants where there would be negligible partial shading conditions [12]. Therefore, the thesis project mainly focuses on the partial shading problem in the rapid growing residential sector where trees, chimneys and neighboring buildings could cast shadow on solar modules, which are inevitable as shown in Figure 1.2.

Figure 1.2: Solar panels under partial shading conditions

When a solar cell in a module is shaded, its generated photo-current will be remarkably reduced [13], thus limiting the power output of the installed PV panel. The shaded solar cell will be operating under reverse bias caused by the other unshaded cells, meaning it will dissipate, instead of generating, energy [6], and this part of dissipated energy is mostly converted into heat. The heat may induce the breakdown of certain solar

cells when their reverse bias are large enough. When the temperature of certain cells exceed normal ranges, the encapsulation materials tend to crack while other materials inside the cell show tendency of wearing out [6], known as the hot-spots, which are believed to permanently damage the performance of solar cells [13]. In addition, the partial shading problem will lead to the electrical mismatch. This mismatch leads to an insufficient annual energy yield of installed PV panels in urban environment.

The previous paragraphs discuss the problems of electrical loss and potential hot-spots due to the partial shading condition. It can be prevented by simply adding bypass diodes into solar panels [14]. Most commonly, these diodes are connected parallel to a number of cells. They block current when solar cells are under reverse bias. However, when one of the cells is shaded, the diode will pass current owing to the biasing from other cells connected in series. The introduction of bypass diodes protects the solar panels, but has the problem of disproportional loss in the same time if the number of bypass diodes are limited.

Most PV panels currently available in the market have all solar cells (6 by 12) connected in series, shown in Figure 1.3, and include 3 bypass diodes [15]. Each bypass diode is connected to a group of 24 cells. When one of the cell is being shaded, the bypass diode connected parallel to this string will be activated and pass the generating current through. The module will experience a decrease of power output around 33 %. Such reduction in power output is much larger than the proportion of the shaded area, which is around 1.67 %.

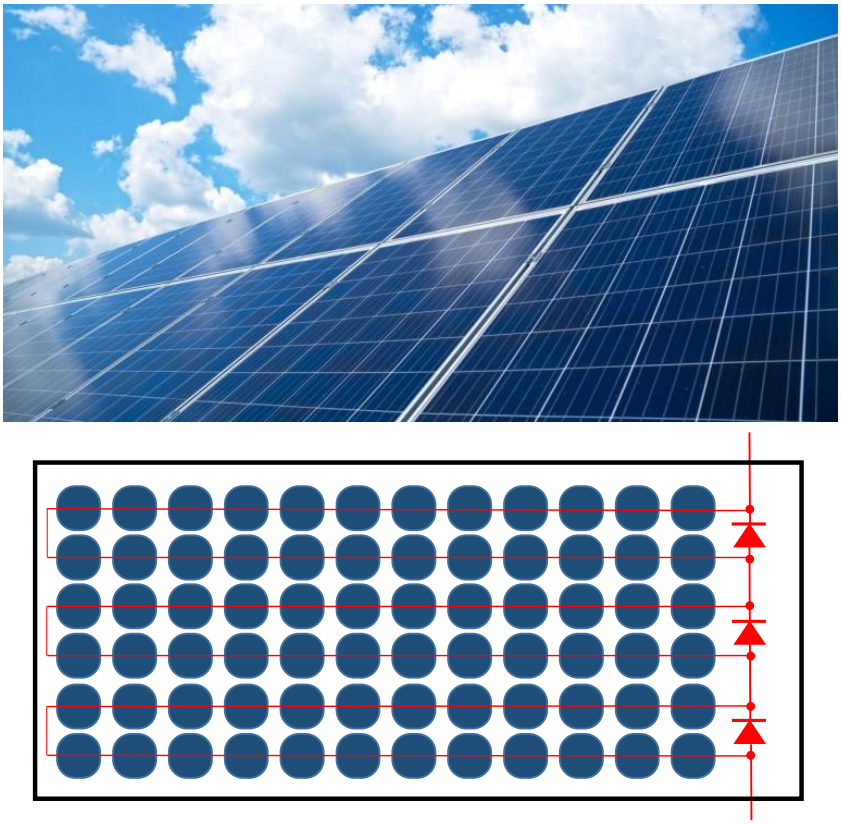

Figure 1.3: Commercial PV panels with 72 cells and 3 bypass diodes

Aside from the 72 cells PV panel, the PV panel consisting 96 cells is shown in Figure 1.4 has 3 bypass diodes as well. Unlike the 72 cells PV panel, half of the cells in the middle are connected parallel to only one diode. Thus, partial shading occurred especially in the middle of the PV panel could lead to a even higher disproportion in this case. A 1.04 % shaded area will lead to a 50 % power output loss.

One straight-forward approach to deal with the disproportional power output losses is assigning one bypass diode to every single solar cell [16]. However, attaching more bypass diodes to a PV panel makes the manufacturing process complex and augments the total cost of certain PV panels.

In addition, there are several cells that could be functioning partially as those with bypass diodes. Attempts have been made on both the front back contacted (FBC) cells and the interdigitated back contact (IBC) cells. When these solar cells are operating under reverse bias, they could become electrically conductive at a relatively low reverse voltage.

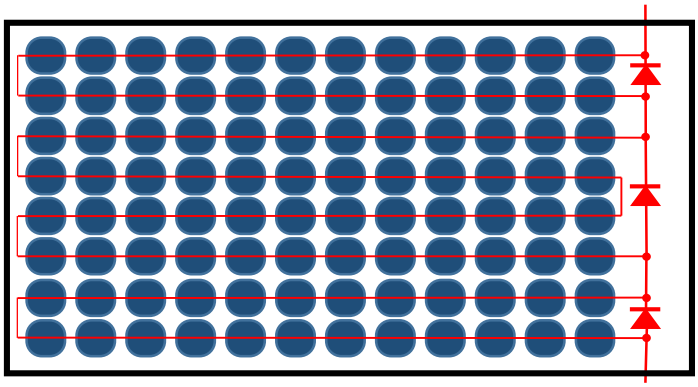

Figure 1.4: PV panels with 96 cells and 3 bypass diodes

The integration of bypass diodes into the FBC cell structure is to create a region with reverse polarity to the bulk [17]. Figure 1.5 below illustrates an integrated bypass diode FBC cell. With a bypass diode region consisted of the same materials listed on the right side, the equivalent circuit of such solar cell will then have an extra bypass diode and a series resistance as shown in Figure 1.6 [17].

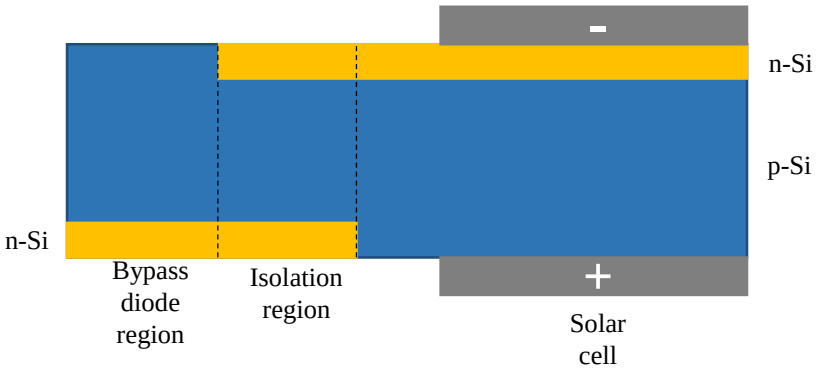

Figure 1.5: Front back contacted cell with integrated bypass diode

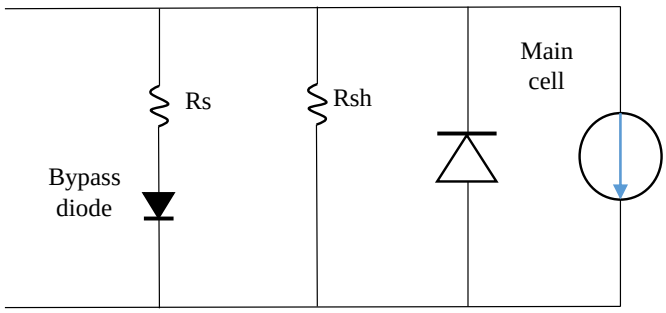

Figure 1.6: Equivalent circuit of a front back contacted cell with integrated bypass diode

When the bypass diode is activated, there will be additional power loss due to the existence of such series resistance. Furthermore, the bypass diode region together with the isolation region occupies too many active areas of the cell, therefore, the efficiency of such bypass diode integrated FBC cell is relatively low [17]. The fabrication process is not convenient as well.

Besides the bypass diode integrated FBC solar cells, other research groups have focused on different types of interdigitated back contact solar cells as well. These IBC cells have high efficiency and low breakdown voltages, below 5 V. The structure of IBC solar cells will be discussed later in chapter 2.

In this case, the PV panels consisting such solar cells are believed to have a better performance under partial shading conditions.

1.4. Problem statement

The problem of partial shading for solar panels has been clarified. Inevitable shading conditions caused by neighboring objects largely limit the annual energy yield of PV modules mounted in urban environment. The introduction of bypass diodes significantly relieves such problem. Bypass diodes are activated when one of solar cells connected in parallel is shaded, thus ensuring the energy output of cells from other strings. However, owing to the limited number of bypass diodes inside the module, there would then be problems of disproportional output losses. In the meantime, different types of solar cells have shown low breakdown voltages and good forward characteristics. Therefore, solar cells without external components but with better shade tolerance are essential.

1.5. Research goal and outline

The rapid expansion of PV installations raises concerns regarding both the high efficiencies and good shade tolerance. Solar cells with low breakdown voltages and high efficiencies remain the trend of future designs. Therefore, the main research goal of this thesis project is to investigate into the most promising cell structure that could maintain high efficiency under forward bias and realize low breakdown voltages under reverse bias at the same time. The research goal can be further divided into three detailed objectives:

1. Investigate different solar cell structures that result in low breakdown characteristics and identify the charge carrier transport mechanisms involved under reverse bias conditions;
2. Generate a robust 2D simulation template to perform a parametric evaluation of the I-V characteristics of a solar cell;
3. Analyze the influence of structural parameters and operating conditions on the forward and reverse I-V characteristics of a solar cell.

This document is structured as follows. Chapter 2 will give an overview of the most common techniques that are used in current state-of-the-art solar cells. This chapter will also introduce the breakdown mechanisms behind each kind of cell structures. Chapter 3 will describe the methods that have been used during the simulation phase of this thesis project. Chapter 4 presents the simulation results concerning the characterisations of different structural factors. Chapter 5 will discuss the effects of realistic working conditions on temperature and irradiance. Finally, chapter 6 presents the conclusions and recommendations. A summary of the most important results obtained during this project will be provided in this chapter while the recommendations for future research will be presented as well.

2

Fundamentals

Before diving into the research project, it is essential to be equipped with several fundamentals. Photovoltaic devices usually process the interaction with light, thus, in this chapter, the basics of solar cell working principles and illustrations of various solar cells will be presented. The breakdown mechanisms will be explained and the reverse characteristics of certain IBC solar cells will be analyzed as well.

2.1. Working principles of solar cells

Nowadays, various photovoltaic technologies have been commercialized and the PV market is in unprecedented prosperity [18]. Among all the technologies, the fundamental working principle of a solar cell is the photovoltaic effect [6].

2.1.1. Generation of charge carriers

The potential of the solar cell is generated over the junction that are formed by two different materials when receiving the electromagnetic radiation. The solar energy incident on Earth, is assumed to be consisted with a flux of photons with different energies. The energy of a photon (E_{ph}) is determined by:

$$E_{ph} = h\nu \tag{2.1}$$

where h is the Plank constant and ν is the frequency of certain electromagnetic radiation. The semiconductor material used to absorb the incident light is characterised by its band gap energy E_G. If the semiconductor material has no defects, electrons are only allowed to occupy a position below the valence band or above the conduction band of certain materials. Such band gap describes the difference between those two energy states:

$$E_G = E_C - E_V \tag{2.2}$$

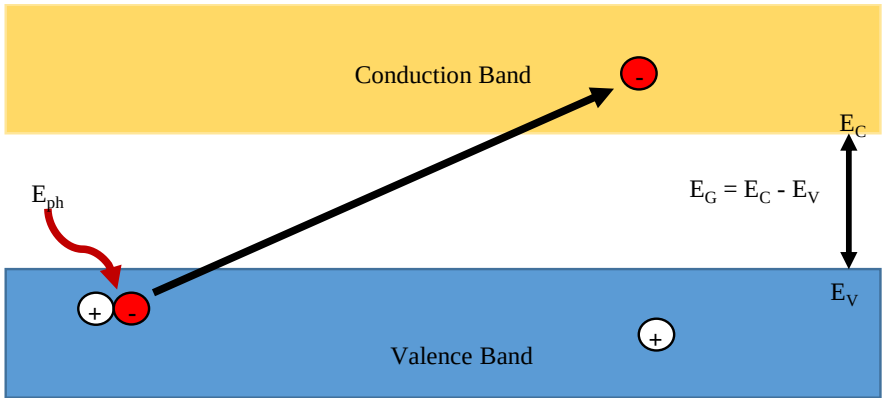

Figure 2.1: The generation of electron-hole pair when an incident light with energy larger than the bandgap of the material

Photons are absorbed by a semiconductor material. The energy of a photon E_{ph} is used to excite an electron from the valence band to the conduction band in such material, which means that a photon is only able to excite an electron into the conduction band when its energy is greater than the band gap energy [19]. The rest of such energy will be dissipated in forms of heat mostly.

2.1.2. Separation and collection of charge carriers

When an electron-hole pair is generated inside the buck region, electrons and holes must be separated and then collected at different contacts of a solar cell to flow through the external load circuit [20]. The flow of charge carriers through the external load builds a DC electric current that can be used to power different electrical devices [6].

Charge carriers flowing through the external circuit usually requires the semipermeable membranes to allow electrons and holes to flow bidirectionally, show in Figure 2.2, and such semipermeable membranes in solar cells are formed by p- and n- materials [6].

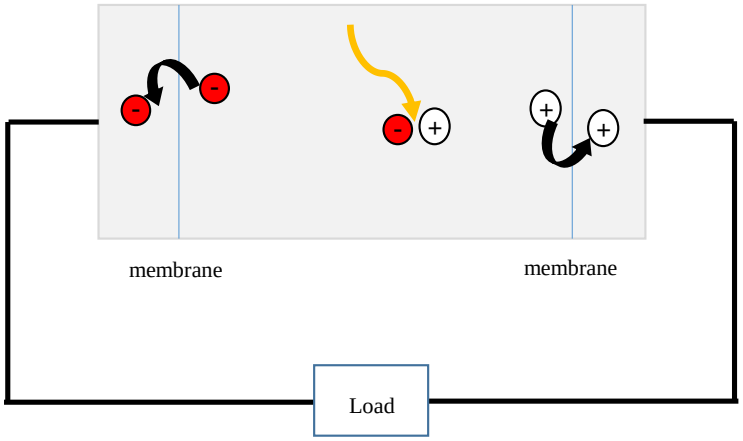

Figure 2.2: Charge carriers separation of simplified cell model

When these two materials are brought together, the different concentrations of holes and electrons form an internal electrical field. The photogenerated electron and hole pairs will then be forced to opposites sides, which is known as the drift current inside the buck region [20]. In the meantime, carriers tend to move from high concentration regions to low concentration regions, known as the diffusion. Such effect will form the diffusion current within such space charge region as well [6]. High concentration of holes at P side and electrons at N side will lead to a diffusion current, and the space charge region will be under equilibrium when the drift current is compensated by such diffusion current [21]. Therefore, doping is used to improve the carrier collections of different materials.

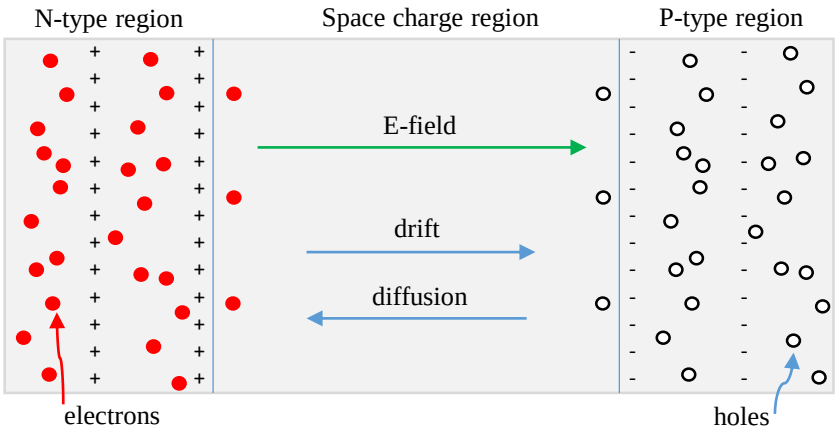

Figure 2.3: Formation of a space charge region and carrier movements

Doping is the manipulation of boron and phosphorus atoms replacing silicon atoms in the structure [22]. When boron is introduced into the silicon based structure, a neighboring electrons will be attached to the boron atom to form bonds towards four neighboring silicon atoms [6]. In consequence, a hole will then be created, which is called the free charge carrier. Such atoms that improve the concentration of holes are called acceptors. Similarly, atoms that can improve the concentration of electrons are called donors, which are often referred to phosphorus [6]. With a high concentration of acceptors and donors, the internal electrical field will be stronger, leading to a higher collection of both photogenerated electrons and holes.

When the doping is introduced, the band diagram of certain materials will be changed correspondingly. The Fermi level, which describes the probability of electrons occupancy at different energy levels, will no longer be at the middle of the bandgap [23]. Instead, the Fermi level will move upwards if the material is doped with phosphorus, or downwards if it is doped with boron. Such changes of Fermi level indicates the property of certain materials, as illustrated in Figure 2.4.

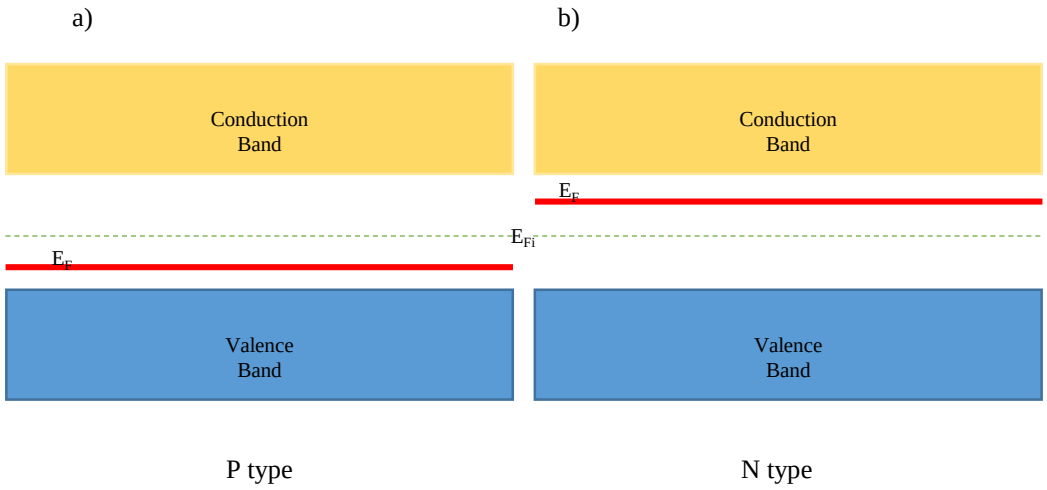

Figure 2.4: Fermi level after a) Boron doping; b) Phosphorus doping

Several metals including aluminium are used to finally collect the photogenerated electron and hole pairs. The metal contacts are placed next to the separation layers and have relatively low resistance [21]. In consequence, the charge carriers flow through the external circuit and will be utilized in different forms.

2.2. Comprehensive complements of solar cells

In this section, various layers of solar cells will be discussed. Most of them are replenished to the structure mentioned above to improve the efficiency of solar cells.

2.2.1. Anti-reflection coating

Anti-reflection coating is placed at the surface of the solar cell. It is the first layer in contact with the incident light. Anti-reflection coating itself has nothing to do with the photon absorption. Such layer is designed to improve the absorption inside the wafer where most of the electron and hole pairs are generated [24].

The flat surface of silicon wafer can have a high surface reflection over 30%. Around one third of the incident light is going to be wasted due to the reflection [20]. Such reflection can be reduced simply by applying a textured anti-reflection coating to the surface. By bouncing the reflected light back to the rough surface, the texturing raises the probability of light refraction into the absorber.

The Fresnel's law describes the intensity of light transmitted and reflected between two medium [25]. It is related to the incident angle and the refractive index of both medium. When an anti-reflection coating is placed in between, the intensity of reflected light will be reduced due to the gradually increasing refractive index from air to the absorber [24]. Therefore, the transmission of incident light will be enlarged with the existence of anti-reflection coating.

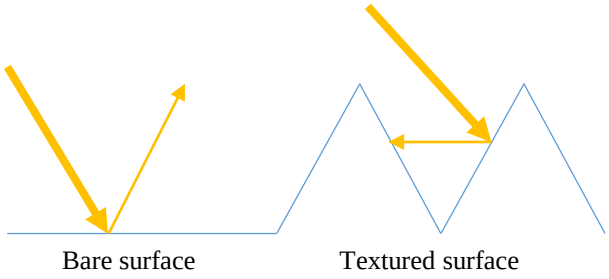

Figure 2.5: Light reflection of bare and textured surfaces

2.2.2. Passivations

Passivations are used in solar cells to prevent the photogenerated electrons and holes from recombining. The periodic crystal of silicon is interrupted at the edges of the wafer [26]. Such edges refer to the interfaces of silicon wafer and other layers in a solar cell diagram. When the periodic crystal is ended abruptly, the formation of allowed electronic states tend to exist at that region. These states can act like effective recombination centers for charge carriers, hence, the collection of photogenerated electron and hole pairs is deteriorated [27].

There are several materials that can be used as the surface passivations. Thin SiO_2, SiNx and Al_2O_3 layers are the main dielectric layers in the state-of-art cell technologies [26]. Under thermal treatment, these layers are able to passivate the silicon dangling bonds. In consequence, the potential recombination centers are reduced and the collection of the photogenerated electron and hole pairs are enhanced [28].

Passivation method is implemented at the interface of metal and semiconductor as well [29], where the recombination velocity is relatively high. The conventional way to passivate this contact is to increase the dopant concentration of certain regions underneath the metal. With a high dopant concentration, electrons and holes will pass the desired boundary, thus reducing the recombination probability at both sides shown in Figure 2.6.

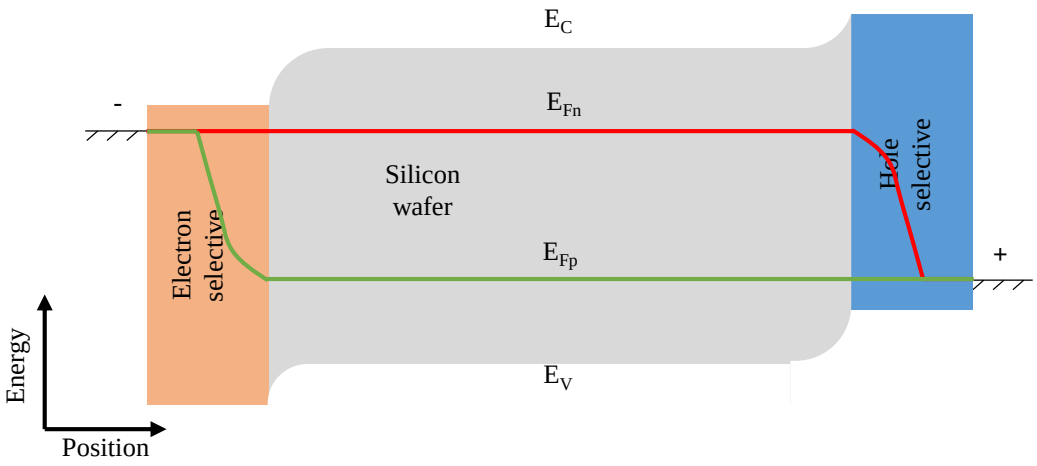

Figure 2.6: Band diagram of c-Si wafer where contacts are passivated by n^+ and p^+ selective regions [26]

2.2.3. Transparent conductive oxides

Transparent conductive oxides layers, TCO in short, are doped metal oxides used in solar cells. TCO layers are usually placed right beneath the anti-reflection coating. TCO layers act as the optically transparent layer for photons incident at the surface to enter the absorber and as the electrically transparent layer for photogenerated electrons or holes to move towards the external circuit.

TCO layers improve the transmission of both photons and charge carriers of the solar cell. Furthermore,

there will be additional parasitic absorption of light with short wavelengths due to the bandgap of TCO [30]. Therefore, TCO layers are widely used in the cell structures nowadays.

2.3. Breakdown mechanisms

Shading conditions are partially inevitable to solar panels operating in urban environment, as mentioned in the first chapter, and will induce the breakdowns of solar cells. The previous sections discuss the working principles and essential components of solar cells. In the following sections, the possible breakdown mechanisms and the performances of two typical solar cells under partial shading conditions will be analyzed.

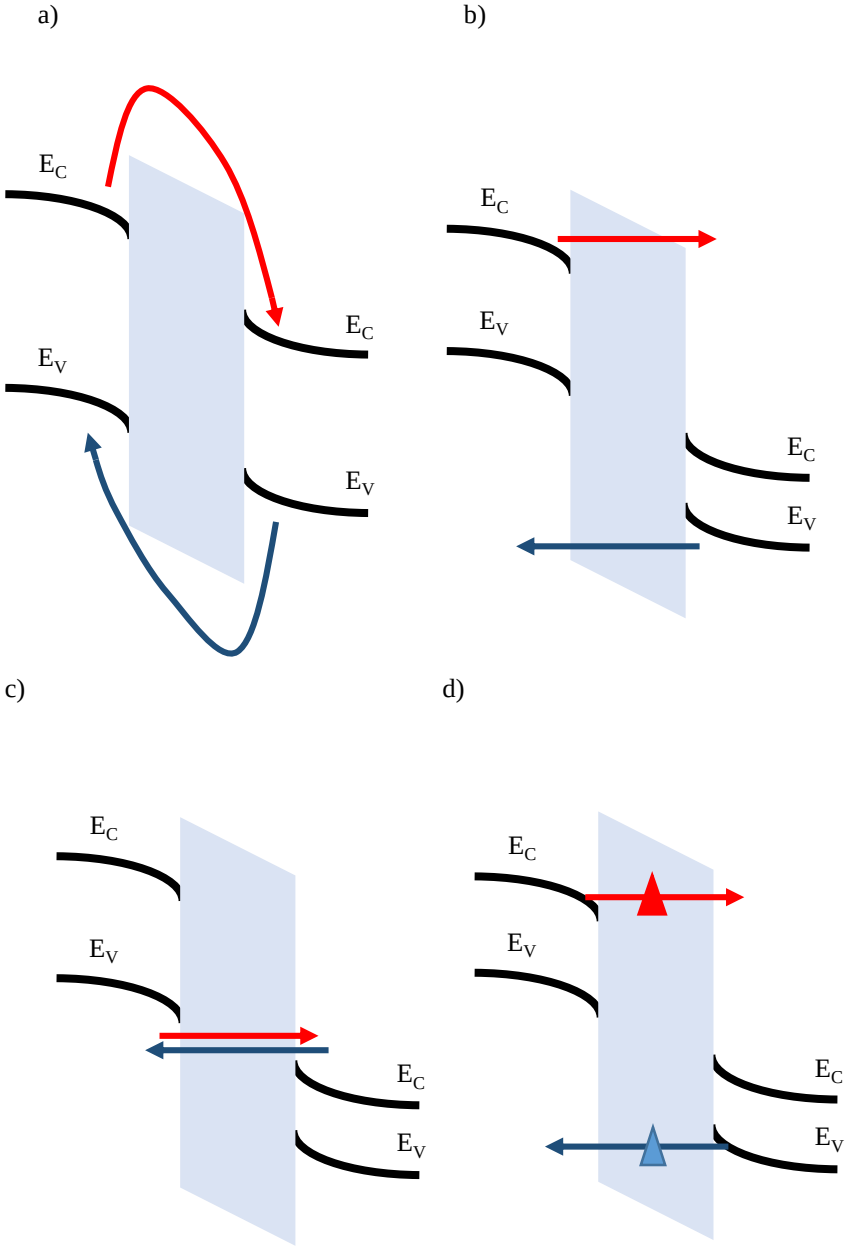

Figure 2.7: a) Thermionic emission; b) Intra band tunneling; c) Band-to-band tunneling; d) Trap assisted tunneling

There are mainly three different types of mechanisms that would lead to the breakdown of the junctions, namely thermionic emission, avalanche breakdown and Zener breakdown [19]. Thermionic mechanism refers to the situation where the carriers are able to overcome the barriers themselves and to be transported, which will not be discussed in this thesis project.

Zener breakdown mechanism describes a different conductive process under reverse bias. It mostly occurs where the electric field of certain region is large enough that the charge carriers start jumping across the narrow junction, and it is also known as tunneling. Tunneling could be further divided into three different types, the trap assisted tunneling, the intra band tunneling and the band-to-band tunneling [31][32]. Most of the trap assisted tunneling happen within the region where there are the presences of traps within the depletion region. The existence of traps, in other words, would split the energy barrier into two parts, resulting in two consecutive tunnel through thinner energy barriers. This would increase the probability of total tunneling process [33]. It is worth mentioning that there could be more than one traps within the barrier especially for those highly degraded junctions. The intra band tunneling and the band-to-band tunneling are both among direct tunneling [32]. Charge carriers could be transported directly through the forbidden energy barrier formed by the dielectric layer in these cases. Such dielectric layers are mostly thin layers compared with the trap assisted tunneling [32]. The main difference between the intra band tunneling and the band-to-band tunneling is that in the intra band tunneling, charge carriers would be transported to the same band after overcoming the barrier while they would be in another band after the band-to-band tunneling process as illustrated in Figure 2.7 [34].

Avalanche breakdown is the dominant mechanism in most crystalline silicon solar cells. The breakdown voltages are usually lager than that of Zener breakdown. A conventional crystalline silicon solar cell has a breakdown voltage over 10 V while the Zener breakdown requires a lower reverse potential [35]. The next section is going to reveal the structures and breakdown behaviors of both FBC and IBC solar cells.

2.4. Front back contacted solar cells

The previous sections provide an overview of essentials in a solar cell and the mechanisms when breakdown occurs. In this section, the most common front back contacted solar cells in the market nowadays will be introduced.

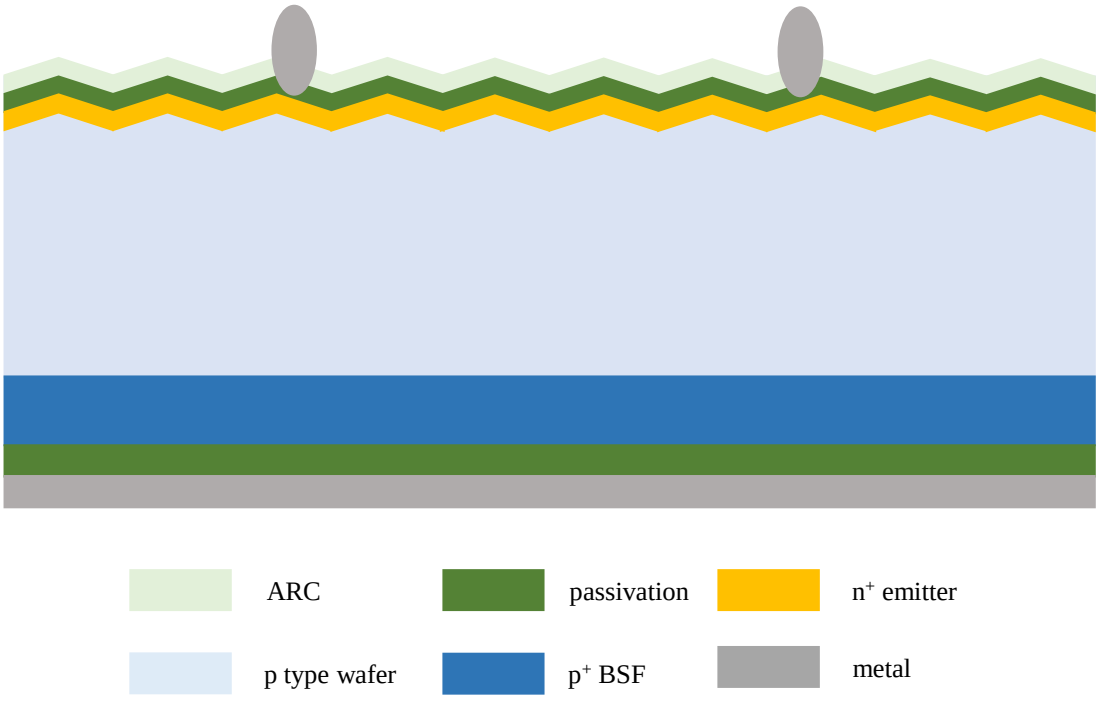

Figure 2.8: Front back contacted solar cell diagram

Front back contacted solar cells have been commercialized in large scales. Such type of solar cells have carrier collection regions on both sides. Figure 2.8 below shows a typical front back contacted cell structure. The incident light reaches the anti-reflection coating and is transmitted through the anti-reflection coating and the passivation layer to the absorber, which is a p type wafer in this case. Photons of wavelength below

1107 nm are absorbed and electron and hole pairs are generated afterwards. The n^+ emitter and p^+ BSF act as the semipermeable membranes for electrons and holes. In consequence, electrons will be then collected at the front side and holes will be collected at the back side. To avoid the possible recombination happening at the interfaces of both n^+ emitter and p^+ BSF between metal contacts, two passivation layer are added to the FBC solar cell. Eventually, collected charge carriers will flow through the external circuit and be utilized in different forms according to the loads.The front back contacted solar cells have advantages of distinct fabrication processes. Layers are grown on top of each other and there are no divisions at a certain depth [20].

2.4.1. Breakdown mechanisms in front back contacted solar cells

Front back contacted solar cells have an internal electric field formed by the P and N junctions as mentioned in the previous section. When solar cells are under reverse bias, such internal electric field is enhanced. As a consequence, the diffusion current will decrease due to a stronger obstacle within the space charge region [20]. When one of the solar cells connected in series is shaded, other unshaded cells will act like a reverse bias on this shaded solar cell. The photogenerated current flowing through this string will be larger than the allowed current passing through this shaded cell. Such shaded cell will eventually become conductive when the reverse bias is large enough, and the required reverse voltage is called the breakdown voltage.

Reverse characteristics can be separated into three different regions based on the the corresponding voltage current behavior [36]. The extremely low breakdown region refers to the situation where ohmic shunts and prebreakdowns are dominate owing to the crystal defects, which is not discussed in this thesis project. Low breakdown region usually correlates to the situation that high recombination occurs when there is tunneling process. The high breakdown region can have a breakdown voltage up to $-60\,\mathrm{V}$. The I-V curve at this region shows a steep slope, which is correlated to the avalanche breakdown mechanisms. The breakdown voltage of most conventional solar cells are among $-10\,\mathrm{V}$ to $-20\,\mathrm{V}$ [36]. The breakdown mechanisms within certain range is avalanche breakdown.

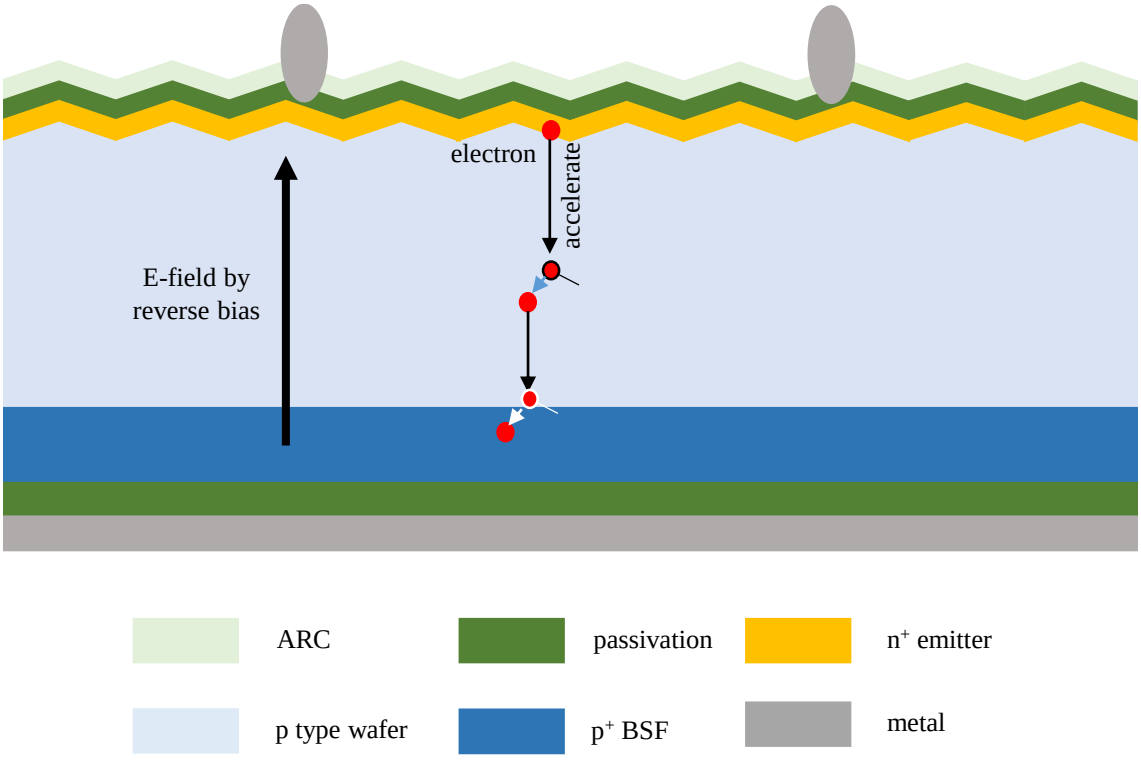

Figure 2.9: Avalanche breakdown mechanism in a front back contacted solar cell under reverse bias

Avalanche breakdown occurs when a high reverse bias is applied. When charge carriers are accelerated by such a strong electrical field, they tend to gain enough kinetic energy to be separated from the covalent bonds. Furthermore, the accelerated carrier will further ionize other atoms on lattice, thus creating extra pairs of electrons and holes. These free carriers further collide with other atoms and produce even more

electron and hole pairs [19]. In the end, the free electrons flowing through the junction and develop the reverse bias current, making the junction electrically conductive. Avalanche breakdown mechanism can lead to a extremely large current within the material which used to be a good insulator [37].

Figure 2.9 shows the avalanche breakdown situation inside a front back contacted solar cell. The electrons are accelerated by the electric field due to the reverse bias and cross the entire wafer,which results in an extremely high breakdown voltage. Other attempts to make front back contacted solar cells become conductive under reverse bias, such as the integrated bypass diode, has been discussed in the first chapter.

2.4.2. Temperature coefficient of breakdown mechanisms in front back contacted solar cells

For avalanche breakdown, the thermal vibration increases and the mean free path decreases at the same time when the temperature increases [35]. In the free path, primary electrons or holes get accelerated strongly enough to knock out electrons from the valence band to the conduction band. Since the path length gets smaller, then the electrons or holes will need larger electric field to acquire kinetic energy equal or greater than the energy gap. To increase the electric means to increase the voltage in this situation. Hence, the breakdown voltage increases with the temperature increase.

2.5. Interdigitated back contact solar cells

Considerable progress has been made in high efficiency silicon based cell technology. Among which comes the concept of interdigitated back contact (IBC) solar cell. The interdigitated back contact solar cells were first introduced by Schwartz and Lammert in 1975 [38]. The most important feature of IBC cells is that all the metal contacts for collecting charge carriers have been moved to the rear side of the device [39] compared with conventional front contact designs illustrated in Figure 2.8. The intention of such modification is to improve the cell efficiency by removing the potential shading losses due to the metal contacts at the front surface. In terdigitated back contact solar cell is the focus of this these project.

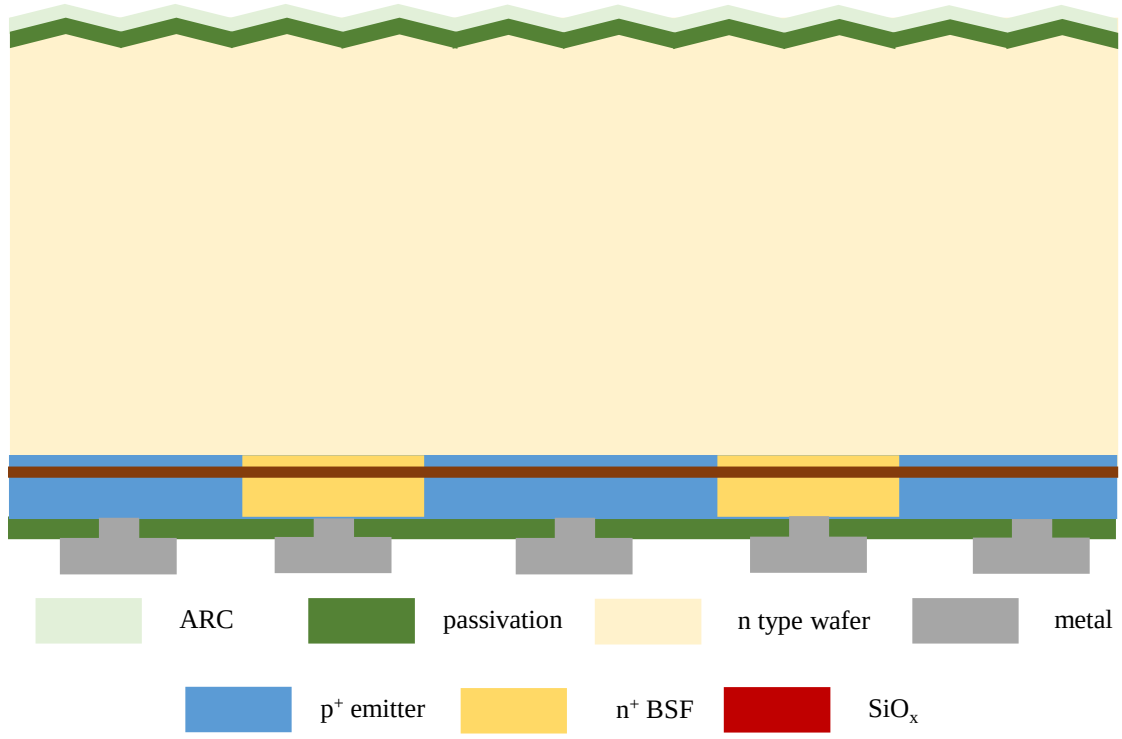

Figure 2.10: Interdigitated back contact solar cell diagram

Figure 2.10 is a specific sketch of an IBC cell structure. On the top of the IBC cell is a anti-reflection coating. This texturing surface is aimed to improve the absorption of incident light on the surface, increasing the possibility of refraction while decreasing the reflection there at the same time. Usually, the anti-reflective

coating together with the transparent conducting oxide layer helps enhance the light transmittance in the solar cells [40]. More light tend to be transmitted to the bulk thus raising the possibility of absorption in the N-type wafer. IBC solar cells have shown unique merits other than its negligible shading losses. The first one is the implementation of monocrystalline float-zone n-type wafers, which would not experience the light-induced degradation [6]. Without the presences of both boron and oxygen, n-type wafer implemented in the IBC solar cells would not suffer from the occurring defects under illumination. Besides, complex fabrication processes of n-type wafer can be avoided for a low sensitivity to the impurities inside the wafer [6], thus resulting in a reasonable price. Furthermore, larger metal fingers for carriers collection can be implemented without concerns of shading. Due to the removal of the surface metalization contacts, the appealing color of the IBC solar cell is decided by the thickness of the anti-reflection coating, which would harmonize with the surrounding constructions and largely promote the utilization of IBC solar cells in different urban environment [41]. A substantial percentage of charge carriers generating near the front surface results in a low front surface recombination velocity [42].The resistive losses at the metallic contacts are reduced as well.

The silicon oxide layer listed between the n type wafer and the interdigitated doped regions has another function beyond passivation, which is to limit the doping diffusion length inside the wafer. The dopant diffusion region inside the n type wafer can lead to a high recombination rate there. The thickness of such silicon oxide layer has been evaluated previously in PVMD group. Silicon oxide layer beyond 1.6 nm would probably forbid the carrier transportation by decreasing the tunneling possibility through this silicon oxide layer while thickness below 1 nm would fail to select the collecting carriers, leading to a high contact recombination in those two heavily-doped interdigitated regions. An appropriate silicon oxide layer here could even improve the transportation of charge carriers and restrict the tunneling for the non-collecting carriers [43]. The interdigitated p^+ and n^+ regions at rear side are formed by high temperature diffusion processes with BBr_3 and $POCl_3$, for instance sputtering [39]. The passivating layer at the rear side is capable of providing excellent passivation on both p^+ and n^+ surfaces as well as withstanding the high temperature fabrication processes. Metals at the rear side are in direct contact with only a small part of doped collection regions thus significantly reducing the recombination processes on the contacting surfaces [41].

IBC solar cells have been commercialized by SunPower company with an efficiency of 24.2 % [6]. In addition, it has been observed that the IBC solar cells have a much better performance under reverse bias. A relatively low breakdown voltage of about −3.7 V at which the reverse current reaches 2 A under dark condition was achieved on a IBC solar cell with a contiguous p+ and n+ region at the rear side [44]. Such soft breakdown behavior suits the need for better resilience against shading precisely.

2.5.1. Breakdown mechanisms in IBC solar cells

Many of the interdigitated back contact solar cells are reported to have breakdown voltages below −5 V. Zener breakdown, due to the high electric field and a short distance, becomes dominant in IBC solar cells at the rear side. Figure 2.11 below presents the reverse characteristics of several IBC solar cells.

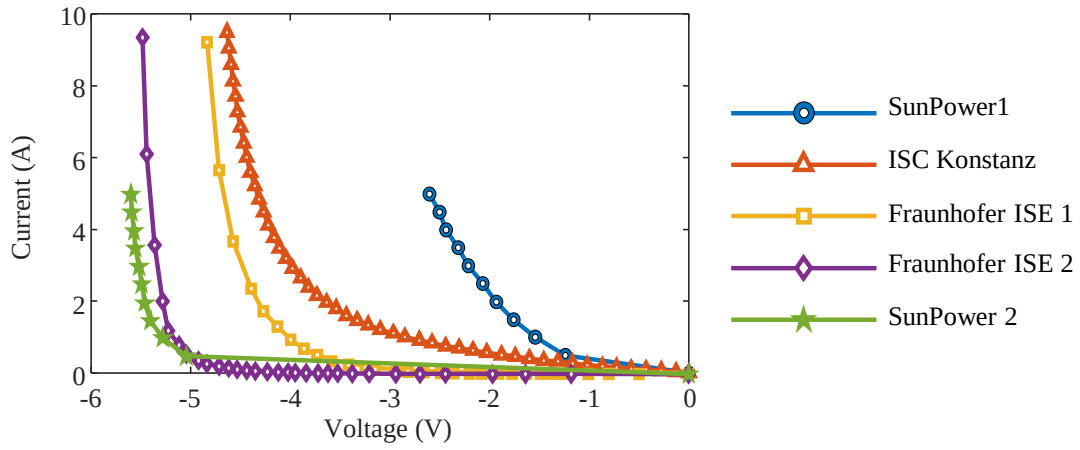

Figure 2.11: Dark I-V reverse characteristics of various solar cells [39][45][46]

Tunneling significantly reduces the breakdown voltage of IBC solar cells and brings such structure to low breakdown region [47]. This is owing to the short distance between p^+ and n^+ regions at the rear side. When

a reverse bias is applied to the cell, tunneling are likely to happen at the rear side. Electrons have a shorter path in IBC cell compared with FBC cells, and the heavily doped p^+ and n^+ regions form a strong electric field, which is beneficial for tunneling at the rear side as well.

The reason for such soft breakdown behavior is the involvement of band-to-band tunneling, in specific. When a heavily doped p+ and n+ junction is under reverse bias, which is exactly the same in this case, electrons can tunnel from the valence band directly into the conduction band. The tunneling current follows

$$J_t \propto A \times F \times V \times \exp(-B/F) \tag{2.3}$$

A and B are positive quantities that are related to material properties such as the bandgap and the effective mass of carriers [44]. F means the average electric field inside the junction and V refers to the applied voltage. The width of the depletion here is small enough, hence, a higher electric field due to the heavily doped p+ and n+ regions at the rear side leads to the desired low breakdown voltage.

A measurement has been carried out on IBC solar cells. The measured IBC cells feature no gaps between the emitter and BSF, which greatly simplifies the process and reduces the manufacturing costs. In the infrared images listed below in Figure 2.12, the area between p+ and n+ regions is relatively uniform which implies that the tunneling current flows through the p^+ and n^+ regions instead of crowding into certain spots [48]. The breakdown over the entire junction tends to be uniform. As the consequence, a uniform heat dissipation is observed. Such measurement confirms a uniform tunneling happening at the rear side. A stable tunneling process leads to a soft breakdown voltage of the device.

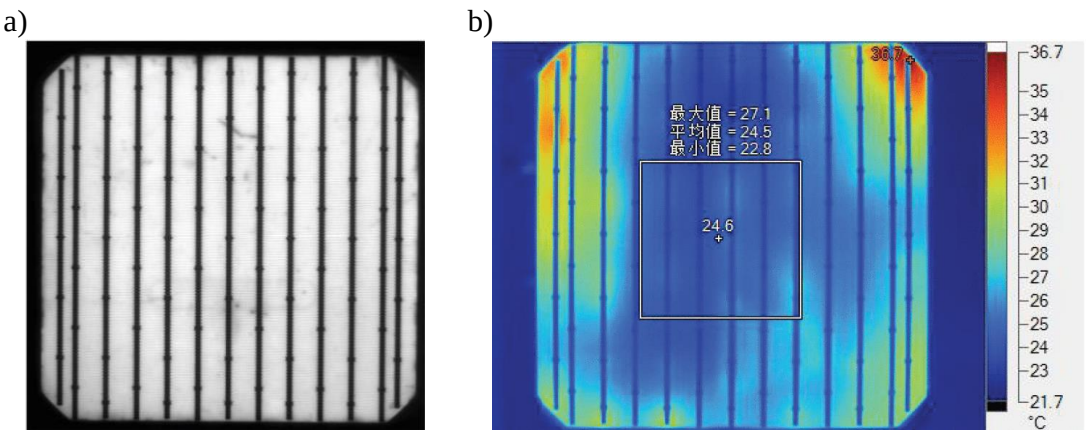

Figure 2.12: a) Photoluminescence image and b) IR characteristics of an IBC solar cell under reverse bias retrived from [48]

2.5.2. Temperature coefficients of breakdown mechanisms in IBC solar cells

For Zener breakdown, the electric field must be sufficiently high to torn electron from the valence band to the conduction band. So, the electric field must be strong enough such that the valence electrons could cross the energy gap. Since the energy gap decreases with temperature increases, then the electric field required to torn the valence electrons decreases with temperature increase, and consequently the required voltage decreases since voltage equals the electric field intensity times the width of the space charge region, resulting in a negative temperature coefficient.

2.5.3. Reverse characteristics of IBC solar panel

A measurement has been carried out in the laboratory to analyze the reverse characteristics of an IBC solar panel. The I-V characteristics of IBC solar panel is measured in the laboratory. Up to 8 cells are being shaded with exactly the same occluder one by one to show the power output of such panel. The results shown in Figure 2.13 confirmed that, unlike the conventional PV panel, the new module made up of low breakdown solar cells would experience power output drops before losing the power generated by the string connected parallel to a bypass diode. The bypass diode would not be activated until more or less 4 cells are being shaded in this experiment.

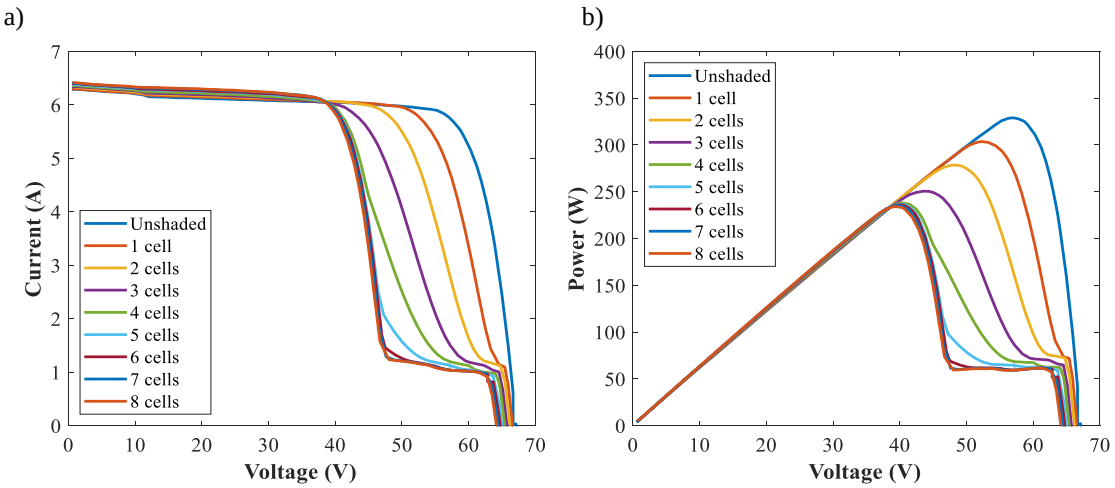

Figure 2.13: Solar module a) I-V and b) P-V plots under different shading conditions

2.6. IBC solar cells with low reverse characteristics

In this section, various interdigitated back contact solar cells will be analyzed. All of them have similar structures and have shown low breakdown voltages.

2.6.1. Maxeon solar cells

SunPower company has commercialized IBC solar cells and has been looking for a large scale of their latest IBC solar cells. The SunPower Maxeon solar cells are the latest cells with both high efficiency and preferable shading tolerance. The state-of-art Gen III cells [45] significantly reduces the breakdown voltage to around −2 V under 2 A current flow, meaning the partial shading condition of a few solar cells in particular will not turn on the bypass diode immediately. The photogenerated current will stay positive under most shading conditions, hence, improving the annual energy yield and PV modules' lifetime.

The state-of-art Gen III cells reduces the surface recombination at the rear side, and the efficiency of such solar cell has reached 24.2 % [45]. A rear mirror has been placed at the back side and the passivation layer there has been textured. Both of them reduces the recombination happening at the rear side surface, thus contributing to a high efficiency and a larger open circuit voltage.

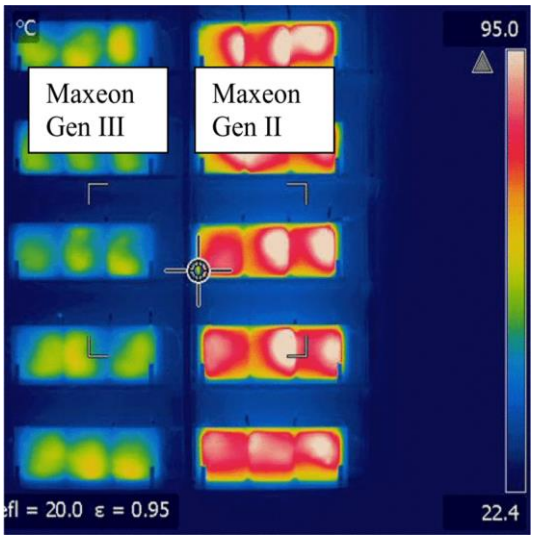

Figure 2.14: Infrared image of Gen III and Gen II IBC solar cells in reverse bias at 5 Amperes under ambient temperature retrieved from [45]

A further investigation of cell performance under reverse bias. The infrared image of Gen III cells shows a lower temperature than the previous IBC cells. The temperature rise in reverse bias at 5 A is around 5 °C. The lower breakdown voltage significantly reduces the heating of the modules, thus enhancing the long term reliability.

2.6.2. IBC-SHJ POLO solar cells

The ISFH research institute has designed the silicon heterojunction IBC cells with polysilicon p^+ and n^+ regions on top of an SiOx layer and such device has an efficiency of 26.1 % [41].

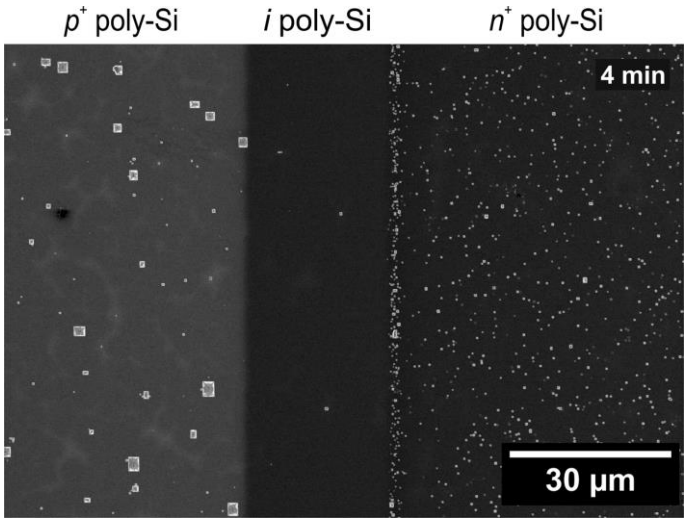

Figure 2.15: SEM images of a p(i)n junction on cell wafer retrieved from [41]

The p^+ and n^+ regions at the rear side is separated by another intrinsic polysilicon layer to avoid recombination process there. The SiOx layer is placed between the n type wafer and the polysilicon regions but has pin holes to allow the collection of generated charge carriers inside the wafer. Such SiOx layer has advantages of good passivation quality of the crystalline silicon surface and low contact resistances as well.

2.6.3. Homojunction IBC solar cells

A research group at Fraunhofer ISE has fabricated IBC solar cells to test the cell performance under both forward and reverse bias. Their simplified fabrication process is combining both ion implantation and furnace diffusion. A local implantation of phosphorus is used to form the n^+ BSF firstly with masks on p side. Then follows a BBr_3 furnace diffusion to form the p^+ emitter and front floating emitter [46].

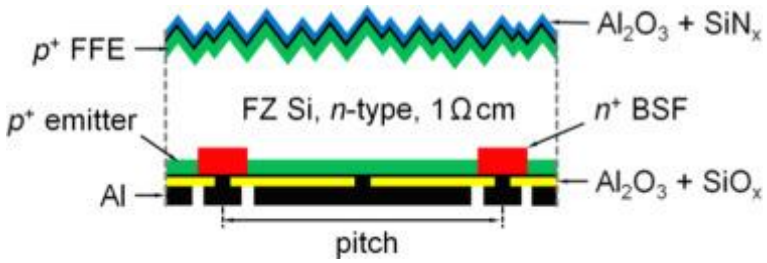

Figure 2.16: IBC solar cell with BSF formed by local ion implantation of phosphorus and subsequent BBr_3 furnace diffusion retrieved from [46]

Such IBC cells have a conversion efficiency up to 22.4 %. The degradation of the device performance is believed to be related to the reduced passivation quality when fabricating. With an finer Al_2O_3 and SiOx or

SiNx passivation layer, the degradation should be controllable [46].

The IBC cells without an interval between p^+ emitter and n^+ BSF at rear side are reported to achieve breakdown voltages around −5 V [46]. The breakdown happens between these two regions and such effect is evenly distributed due to a uniform doping level throughout the region, which is similar to other IBC solar cells discussed in the previous sections. Moreover, different doping profiles have limited influences on the reverse breakdown voltages of the device.

2.6.4. Soft breakdown IBC solar cells

Another IBC solar cell with low reverse characteristics designed by the research group in ISC Konstanz suggested a non-separation doped regions at the rear side. The heavily doped p+ and n+ regions are placed next to each other and the corresponding breakdown voltage under reverse bias could reach −3.7 V [44]. The simulation carried out indicates a band-to-band tunneling across the borders of p^+ and n^+ regions at the rear side. The breakdown inside these IBC solar cells are uniform over the entire device and, most importantly, is non-destructive.

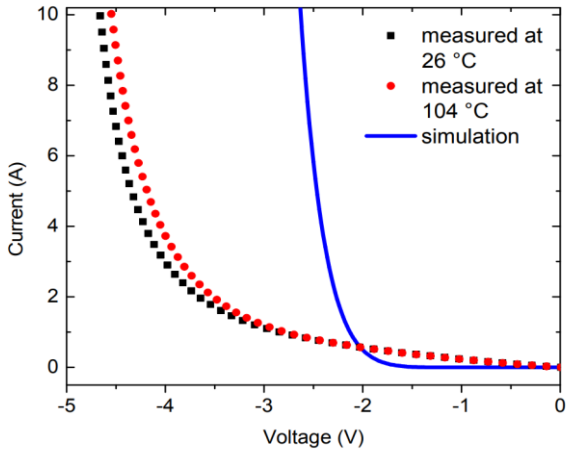

Figure 2.17: Measured reverse IV curves at different temperatures retrieved from [44]

A measurement of two dark I-V curves at 26 °C and 104 °C shows a negative temperature coefficient of such device. Such negative temperature coefficient strongly supports the tunneling mechanisms within the device as discussed in the previous sections [35]. In the meantime, the study of dopant concentrations influences on the breakdown characteristics has been carried out. The breakdown voltage can be modified by changing the dopant profiles. When the boron or phosphorus sheet resistance is reduced, both the efficiency and the breakdown voltage can be improved.

2.7. Reflections

In this chapter, the fundamental working principle of solar cells, the photovoltaic effect, is introduced. Solar cells absorb light with energy greater than the bandgap to generate electrons and holes. Electrons and holes are then collected at doped p and n regions to flow through an external circuit. The designs of anti-reflection coating, passivations and transparent conductive oxides are for higher energy conversion efficiency of the cell. When solar cells are partial shaded, they will be under reverse bias conditions and breakdowns can happen. Avalanche breakdown remains dominant in front back contacted solar cells, resulting in relatively high breakdown voltages due to the long distance of p and n regions. Tunneling is the key mechanisms for the low breakdown voltage interdigitated back contact cells, where both p and n regions are placed at the rear side. IBC solar panels tend to harvest more energy than the conventional FBC panels because of the low breakdown voltages. Different designs of IBC cells are reported to achieve high efficiency and low breakdown voltages at the same time.

Interdigitated back contact solar cells, as explained in the previous chapters, are among the most promising cell structures in the low breakdown voltages field. The IBC solar cells with contiguous p^+ and n^+ regions

can realize a breakdown voltage towards −3.7 V [39]. It has been revealed in Equation 2.3 that a higher electric field would lead to a higher tunneling probability through the depletion region at the rear side. However, if there is no separation between those two heavily doped p^+ and n^+ regions, they will get in touch with each other, causing shunting not only at the rear side but also within the wafer where there are two dopant diffusion regions and destroying the forward characteristics.

In consequence, an silicon heterojunction interdigitated back contact solar cells similar to the structure studied in section 2.6.2 is selected with an intrinsic polysilicon layer inserted into the gap between p^+ and n^+ regions to suppress the recombination flowing through.

3

Device Simulation

In this chapter, the simulation tools are presented according to the procedures. Physical models involved and reasons for activating these models will be explained.

3.1. Simulations of solar cells in Sentaurus TCAD

Sentaurus TCAD is an advanced multidimensional device simulator with a broad category in different simulations, including electrical, thermal, and optical characteristics, of silicon based and compound semiconductor devices [49]. It is chosen to simulate the electrical performance of silicon based interdigitated back contact solar cells for its comprehensive functions and capability of new device simulation for which fabrication processes are not yet defined [50]. Majority of the thesis project simulations and sensitivity analysis are carried out in Sentaurus.

3.2. Generation of geometric structures in Sentaurus structure editor

Sentaurus structure editor is a two dimensional or three dimensional structure editor to create TCAD devices. Device structures are generated while dopant concentration profiles and meshing strategies are defined interactively in Sentaurus structure editor. The geometry operations in Sentaurus are based on the ACIS geometry kernel [50].

Figure 3.1 shows a promising cell structure in Sentaurus simulations. An silicon heterojunction interdigitated back contact solar cells similar to the structure studied in section 2.6.2 is created by Sentaurus structure editor. The parameters defined and modified in the structure editor are listed below in Table 3.1.

Table 3.1: Parameters in Sentaurus structure editor

IBC solar cells structure parameters			
Cell pitch	600 µm	ARC thickness	5 nm
Wafer thickness	260 µm	SiOx layer thickness	1.2 nm
P^+ region width	518 µm	P^+ region thickness	20 nm
intrinsic polysilicon layer width	1 µm	intrinsic polysilicon layer thickness	20 nm
N^+ region width	81 µm	N^+ region thickness	20 nm
Metal contact width (P^+)	498 µm	Metal contact thickness (P^+)	10 µm
Metal contact width (N^+)	62 µm	Metal contact thickness (N^+)	10 µm
Wafer Phosphor concentration	$1.559 \times 10^{15} cm^{-3}$	P^+ boron concentration	$10^{20} cm^{-3}$
N^+ boron concentration	$10^{20} cm^{-3}$		

Other parameters such as the doping profiles and meshes are defined in structure editor as well. Sentaurus solves the continuity equations inside each mesh element so that the meshing sizes are finer closer to the interfaces and regions with large doping gradients. The doping profiles consider the lateral penetration and vertical diffusion are considered and follows Gaussian distribution at certain regions.

The optical simulation is carried out with GenPro4 in advance [51]. Such simulation results are loaded in Sentaurus and photon absorption at every depth of the solar cell is assigned as an input. Therefore, the

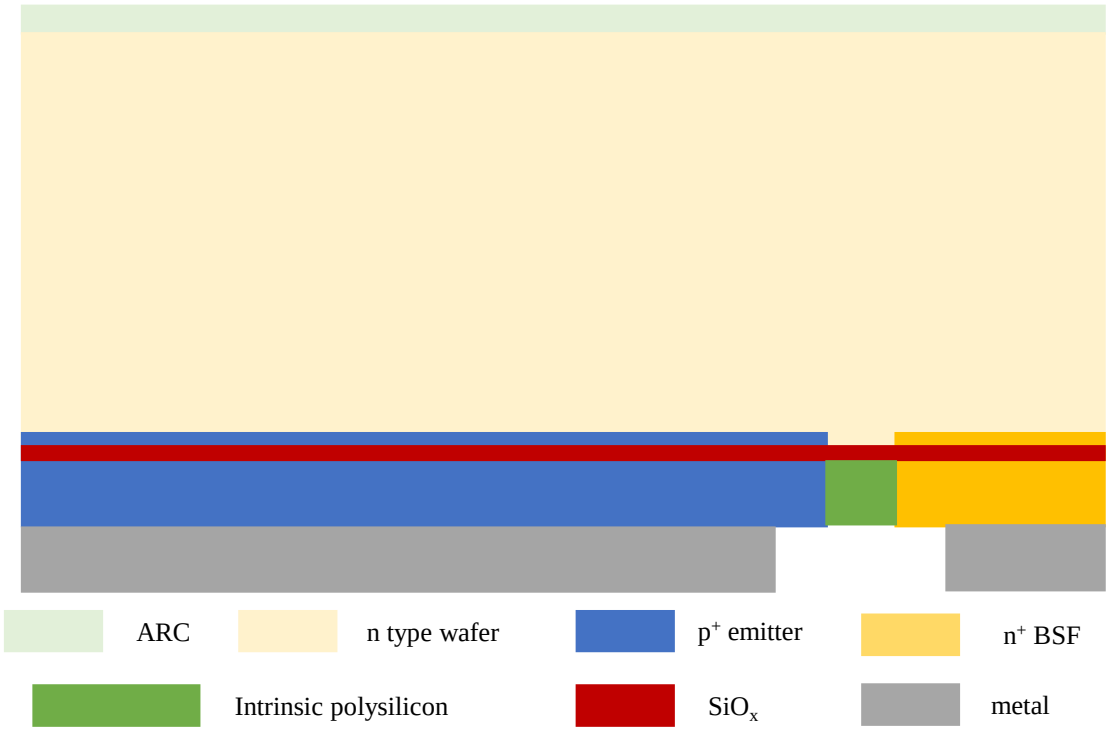

Figure 3.1: Diagram of the IBC-SHJ solar cell

anti-refection coating and the passivation layers are eliminated because they only complicates the meshes for electrical simulations. The optical effect of texture is included in the optical generation profile loaded in Sentaurus.

3.3. Physics in Sentaurus device

Sentaurus device functions as the circuit simulator for the two dimensional semiconductor device generated in Sentaurus structure editor. In this chapter, different physical models and fundamental physics are introduced for the electrical simulation.

3.3.1. The poisson equation and quasi Fermi levels

In all semiconductors, both the mobile and immobile charges like the traps and ionized dopants are of vital importance. The electrostatic potential determined by all kind of the chargers remain the fundamental parts of device simulations and is the solution of the Poisson equation [49] :

$$\nabla \cdot (\varepsilon \nabla \phi + \overrightarrow{P}) = -q(p - n + N_D - N_A) - \rho_{trap} \tag{3.1}$$

where:

- ε is the electrical permittivity.
- $\overrightarrow{P}$ is the ferroelectric polarization, which is linearly dependent on the electric field $\overrightarrow{F}$.
- q is the elementary electronic charge.
- n and p are the electronic charge.
- N_D and N_A are the concentration of ionized donors and acceptors.
- ρ_{trap} is the charge density contributed by traps and fixed charges.

When contacts are at the same potential, the device is under equilibrium .The electron and hole densities can be calculated based on the corresponding quasi-Fermi level [49]. The formulas of the densities are:

$$n = N_C \exp\left(\frac{E_{F,n} - E_c}{kT}\right) \tag{3.2}$$

$$p = N_V \exp\left(\frac{E_V - E_{F,p}}{kT}\right) \tag{3.3}$$

under Boltzmann statistics, where:

- N_C and N_V are the effective density of states in the conduction and valence bands, respectively.
- E_C and E_V are the conduction and valence band edges, defined as:

$$E_C = -\chi - q(\phi - \phi_{ref}) \tag{3.4}$$

$$E_V = -\chi - E_{g,eff} - q(\phi - \phi_{ref}) \tag{3.5}$$

  where χ is the electron affinity, $E_{g,eff}$ is the effective band gap, and ϕ_{ref} is a constant reference potential.

- $E_{F,n} = -q\Phi_n$ and $E_{F,p} = -q\Phi_p$ are the quasi-Fermi energies for electrons and holes, Φ_n and Φ_p are respectively the electron and hole quasi-Fermi potentials.

Boltzmann statistics utilizes the results of Maxwell law of distribution and Boltzmann theorem relating entrophy and probability [52]. Quantum statistics has been developed by Fermi to apply to indistinguishable identical particles having spin half [53]. The dopant concentrations of both P and N regions in this simulation are 10^{20}cm^{-3} as mentioned in the previous section, so Fermi statistics would then be more accurate than Boltzmann statistics [54]. Equations 3.2 and 3.3 are then replaced by:

$$n = \gamma_n N_c \exp\left(\frac{E_{F,n} - E_C}{kT}\right) \tag{3.6}$$

$$p = \gamma_p N_V \exp\left(\frac{E_V - E_{F,p}}{kT}\right) \tag{3.7}$$

where γ_n and γ_p are given by:

$$\gamma_n = \frac{n}{N_C} \exp\left(\frac{E_{F,n} - E_C}{kT}\right) \tag{3.8}$$

$$\gamma_p = \frac{p}{N_V} \exp\left(\frac{E_V - E_{F,p}}{kT}\right) \tag{3.9}$$

- n and p are the electronic charge.
- N_C and N_V are the effective density of states in the conduction and valence bands, respectively.
- E_C and E_V are the conduction and valence band edges.
- $E_{F,n}$ and $E_{F,p}$ are the quasi-Fermi energies for electrons and holes.

Within an ideal cell structure, two different junctions end abruptly at the interfaces. The conduction or the valence bands near an abrupt heterointerface are not aligned, which is known as the discontinuous interface in Sentaurus simulations [49]. This usually occurs on the heterointerfaces of different layers. The continuous quasi-Fermi potential is essential in the simulations as it indicates the state of equilibrium. Therefore, heterointerface model together with the thermionic-emission model, which defines the possible thermionic current and energy flux through the interfaces, have been switched on in the device simulation [55] to ensure a continuous condition.

3.3.2. Carrier transport in semiconductors

Different transport models are used in device simulations including drift and diffusion model, thermodynamic model, hydrodynamic model and Monte Carlo model [49]. The main carrier transport model used is thermodynamic model, which is suitable for a low thermal exchange and high power density devices [56]. The fundamental working principle of carrier transport model is the continuity equations:

$$\nabla \cdot \overrightarrow{J_n} = qR_{net,n} + q\frac{\partial n}{\partial t} \tag{3.10}$$

$$-\nabla \cdot \overrightarrow{J_p} = qR_{net,p} + q\frac{\partial p}{\partial t} \tag{3.11}$$

where:

- n and p are the electron and hole density, respectively
- $R_{net,n}$ and $R_{net,p}$ are the net recombination rate of electrons and holes, respectively
- $\overrightarrow{J_n}$ and $\overrightarrow{J_p}$ are the current densities of electrons and holes, respectively

The continuity equation is the fundamental equation that describes the carrier transport model in the simulation, additional equations regarding electron and hole temperature effects on carrier transport are not included [57]. The only temperature simulation that will be carried out in this thesis is the lattice temperature, which will be discussed in chapter 5 later.

Boundary conditions together with electrical properties are essential in solving continuity equations. They come after the definition of carrier transport models. Contacts on semiconductors in this simulation template are Ohmic contacts by default, with a resistance of 1 mΩ when connected to a circuit node [58]. There is no resistance in other conditions. Charge neutrality and equilibrium are assumed at Ohmic contacts. The conditions are written as:

$$n_0 - p_0 = N_D - N_A \tag{3.12}$$

$$n_0 p_0 = n_{i,eff}^2 \tag{3.13}$$

where n_0 and p_0 are the equilibrium concentrations of electron and hole, respectively. $n_{i,eff}$ refers to the effective intrinsic density, which takes into account the doping dependent bandgap narrowing.

3.3.3. Carrier mobility

Definition of carrier mobility in Sentaurus device takes both carrier scattering and mobility degradation into account. It implements a modular approach for the description of the carrier mobilities. For the doped materials, the carriers scatter with the impurities, which leads to a degradation of the mobility [59]. Both the n type wafer, p^+ and n^+ regions at the rear side have been doped. Therefore, the Philips unified mobility model is switched on to describe not only the temperature dependence but also the electron-hole pairs scattering and the impurities screening and clustering [49]. According to Matthiessen's rule:

$$\frac{1}{\mu_{i,b}} = \frac{1}{\mu_{i,L}} + \frac{1}{\mu_{i,DAch}} \tag{3.14}$$

The Philip unified mobility model has two contributions namely $\mu_{i,L}$, which represents the lattice scattering, and $\mu_{i,DAeh}$, which represents all other bulk scattering mechanisms owing to ionized particles and free carriers [60]. $\mu_{i,L}$ is relevant to temperature and can be calculated according to Equation 3.15:

$$\mu_{i,L} = \mu_{i,max}\left(\frac{T}{300}\right)^{\theta_i} \tag{3.15}$$

The definition of $\mu_{i,DAeh}$ is complicated and contains the effects of clustering of donors and acceptors. Mobility degradation at interfaces are not used in the study because of the flat surfaces built in geometric structure in Sentaurus structure editor.

In other regions where the materials are not doped, the carrier drift velocity is no longer proportional to the electric field. On the contrary, the velocity saturates to a finite speed v_{sat}. The saturation velocity is described by the extended Canali model [61]. The extend Canali model indicates that saturation velocity v_{sat} is proportional to the initial value, which is measured when the temperature is 300 K.

3.3.4. Band structure of semiconductors

For semiconductor deviced simulations, essential properties other than electrostatic potential and carrier transport is the band structure. It is complicated in real situations to simulate the accurate band structures that Sentaurus has simplified it to four important parameters named the energies of the conduction and valence band edges and the density-of-states masses for electrons and holes [49]. For undoped semiconductors, the band gap and the density-of-state masses are determined by the intrinsic density n_i:

$$n_i(T) = \sqrt{N_C(T)N_V(T)}\exp\left(-\frac{E_g(T)}{2kT}\right) \tag{3.16}$$

The bandgap is dependent on temperature [62]. Basically, the rise of temperature causes a decrease in bandgap energy of silicon based semiconductors. Therefore, $E_g(T)$ accounts for the temperature dependent bandgap energy. The bandgap narrowing could be switched off on remaining materials, for example the silicon oxide layer, based on its property. The bandgap narrowing in silicon and poly-silicon regions in the template is specified by using a function of donor and acceptor concentrations. The total bandgap narrowing is the sum of the contributions of the two dopant types [63]. The density-of-state masses for electrons and holes are also considered to be temperature dependent:

$$m_n = 6^{2/3}\, a\, m_0^{2/3}\frac{E_g(0)}{E_g(T)}m_1^{1/3} + m_m \tag{3.17}$$

$$\frac{m_p(T)}{m_0} = \frac{a + b\,T + c\,T^2 + d\,T^3 + e\,T^4}{1 + f\,T + g\,T^2 + h\,T^3 + i\,T^4}^{2/3} + m_m \tag{3.18}$$

where

- coefficients from a to i are all default values listed in Table 3.2.
- m_m is used to define the temperature dependent m_p and m_n [64].

Table 3.2: Default coefficients for effective mass model

Default coefficients for effective mass model		
Parameter name	**Value**	**Unit**
a	0.4435870	1
b	0.3609528×10^{-2}	K^{-1}
c	0.1173515×10^{-3}	K^{-2}
d	0.1263218×10^{-5}	K^{-3}
e	0.3025581×10^{-8}	K^{-4}
f	0.4683382×10^{-2}	K^{-1}
g	0.2286895×10^{-3}	K^{-2}
h	0.7469271×10^{-6}	K^{-3}
i	0.1727481×10^{-8}	K^{-4}

3.3.5. Generation and recombination processes

The carriers, other than undergoing the drift and diffusion process as discussed in the previous sections, are affected by the generation-recombination process as well. In high defect density regions, Shockley-Read-Hall recombination process is the dominant mechanism of carrier transport [65]. The trap-assisted Shockley-Read-Hall recombination is highly sensitive to the energy differences between the defect level and the intrinsic level. With respect to the dopant concentrations and the temperature, the recombination rate is written as:

$$R^{SRH} = \frac{np - n_{i,eff}^2}{\tau_p(n + n_1) + \tau_n(p + p_1)} \tag{3.19}$$

$$n_1 = n_{i,eff}\exp\frac{E_{trap}}{kT} \tag{3.20}$$

$$p_1 = n_{i,eff} \exp - \frac{E_{trap}}{kT} \tag{3.21}$$

E_{trap} refers to the difference between the intrinsic and defect level. It can vary from a wide range depending on the trap density. In Sentaurus, the default value is chosen to be 0 for silicon layers. $n_{i,eff}$ is the effective intrinsic density, which takes into account the doping dependent bandgap narrowing [49].

The surface recombination model is activated at the interfaces. The model used is structurally equivalent to the Shockley-Read-Hall recombination process described above [66]. The surface recombination equations are written as:

$$R_{surf}^{SRH} = \frac{np - n_{i,eff}^2}{s_p(n + n_1) + s_n(p + p_1)} \tag{3.22}$$

$$n_1 = n_{i,eff} \exp \frac{E_{trap}}{kT} \tag{3.23}$$

$$p_1 = n_{i,eff} \exp - \frac{E_{trap}}{kT} \tag{3.24}$$

The equations are modified in the same way as for bulk Shockley-Read-Hall recombination. The only difference is the recombination velocity s is dependent on the concentrations of dopants at the surface.

The recombination rate of band-to-band Auger recombination is written as:

$$R_{net}^{A} = \left(C_n n + C_p p\right)\left(np - n_{i,eff}^2\right) \tag{3.25}$$

C_n and C_p are two temperature dependent Auger coefficients and increase with temperature. Auger recombination is typically important when the dopant concentration is high, which is exactly the same in this simulation template [67]. Therefore, the recombination current output mostly relies on Auger recombination in this simulation template. Radiation recombination is negligible in this case.

3.3.6. Band-to-band tunneling

Tunneling models are selectively switched on when there is possibility of conductivity. Band-to-band tunneling model has been switched on vertically through the silicon oxide layer and lateral through the intrinsic polysilicon layer. The non-local tunneling model defines the starting position of band-to-band tunneling and draws a straight line opposite to the gradient of the valence band at the starting position [49]. The potential tunneling energy is equal to the conduction band energy plus the band offset at the ending position. Tunneling mass represents the probability of tunneling within a certain region. When the tunneling mass of the conduction band $m_(C)$ and valence band $m_(V)$ increases, the tunneling probability will decrease as a consequence.

The band-to-band tunneling is modeled using the following equation:

$$R_{net}^{bb} = A\, F^{7/2} \frac{\widetilde{n}\widetilde{p} - n_{i,eff}^2}{(\widetilde{n} + n_{i,eff})(\widetilde{p} + n_{i,eff})} \left(\frac{F_C^{\mp -3/2} \exp\left(-\frac{F_C^{\pm}}{F}\right)}{\exp\left(\frac{\hbar\omega}{kT}\right) - 1} + \frac{F_C^{\pm -3/2} \exp\left(-\frac{F_C^{\mp}}{F}\right)}{1 - \exp\left(-\frac{\hbar\omega}{kT}\right)} \right) \tag{3.26}$$

The Schenk model above describes the tunneling happens within the steep p-n junction or the strong electric field regions. The $\widetilde{n}$ and $\widetilde{p}$ are two density correction parameters compared with n and p. $F_C^{(}\pm)$ and $F_C^{(}\mp)$ are the critical field strengths. The upper sign in the equation above is the tunneling generation and the lower sign refers to the recombination process [57]. Physically, the band-to-band tunneling occurs within a certain distance. The tunneling path longer than this value would decrease the reliability of the Schenk model. The insulator made up of silicon oxide can be extremely difficult for band-to-band tunneling, but the relatively small width, which equals 1.2 nm enables the tunneling through the layer.

3.4. External circuit connections in Sentaurus

An external circuit must be applied on the solar cell to simulate its I-V curve [49]. Two virtual electrodes are created and placed right at the middle of the metal contacts for such intention. With the existence of the external circuit, the designs of solar cells could be evaluated by key parameters, for instance the open circuit voltage (V_{oc}) and the fill factor (FF). The entire two dimensional simulation template presents a cross section of the solar cell and its link to the external direct current circuit. Simulation takes advantages of the symmetry of solar cells to simulate a 2D device. The default length of this two-dimension model is set to be 1 µm if necessary, thus, the calculations of certain parameters, such as photon absorption, can be carried out.

3.5. Reflections

Overall, the simulation process of IBC solar cell in the Sentaurus has been explained together with the physical models implemented. Geometric structure is generated in Sentaurus structure editor. Sentaurus device simulates the physical processes from electrostatic potential to the generation and recombination processes. Most of the physical models require fitting parameters which mostly come from the experiments in the laboratory. Different correction factors are implemented in models and are used for various situations.

4

Simulations of structural parameters

In the previous chapters, the review of the interdigitated back contact solar cells and the working principles in Sentaurus have been presented. In this chapter, analysis of structure parameters will be presented. Effects of such parameters on breakdown voltages are indicated as well in this chapter.

4.1. Gap region between the emitter and the BSF

The initial simulation is based on the assumption that the interface between the doped polysilicon region and the intrinsic polysilicon region is abrupt.

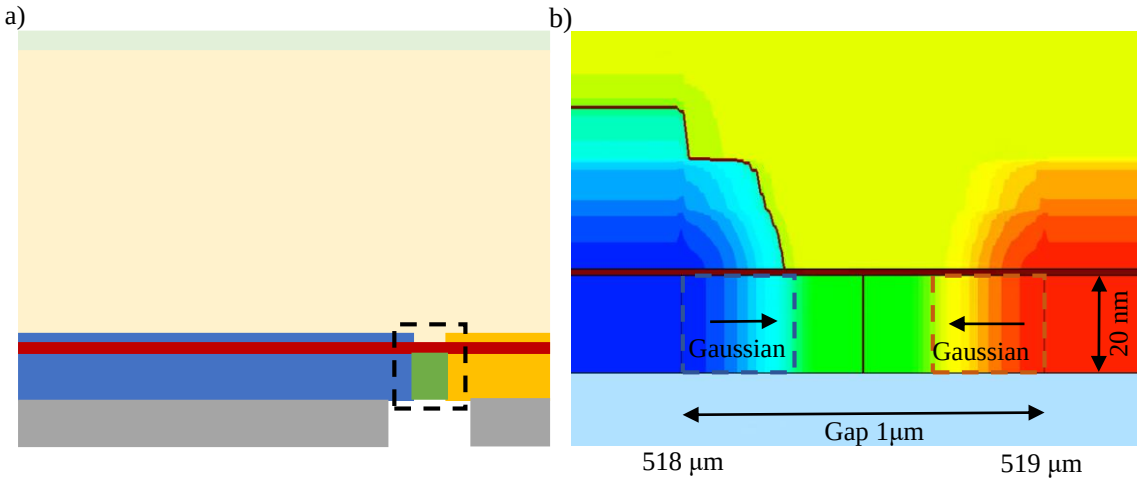

Figure 4.1: a) IBC cell diagram; b) Structure of IBC solar cell at the gap region

The structure of an IBC solar cell is shown together with the details at the rear side in Figure 4.1. Both the p^+ and the n^+ regions at the rear side extend their dopant penetration regions laterally into the intrinsic polysilicon layer, marked with boxes, just like the dopant diffusion regions inside the n type wafer. The fabrication process forms a gap between the heavily doped p^+ and n^+ regions. An intrinsic polysilicon layer is there to suppress recombination process within the gap region. Such intrinsic polysilicon is in direct contact with p^+ and n^+ regions and has no isolation layer in between. In consequence, their penetration regions into the intrinsic poly-silicon layer act in accordance with Gaussian distribution in horizontal axis and can be controlled by state-of-art fabrication processes. This results in a compensated poly-silicon region.

The compensated poly-silicon indicates the almost same concentrations of boron and phosphorus inside this region, hence, it is no longer intrinsic. In order to distinguish from the vertical diffusion inside the N type wafer, dopant penetration regions are used to describe the lateral diffusion inside the intrinsic polysilicon region. The existence of silicon oxide layer limits the diffusion length inside the wafer while the penetration

length inside the intrinsic layer would be longer owing to the lack of silicon oxide layer functioning insulation. The updated structure within the gap region consequently improves the accuracy of the simulation model and is more similar to the IBC solar cell in reality. The following sections will analyze the compensated polysilicon region.

4.2. Tunneling between the emitter and the BSF

Tunneling usually happens where the electromagnetic field is intense and the tunneling path is short. The most possible carrier transportation at the rear side of the IBC solar cells is direct tunneling. It happens between two carrier selective layers, the emitter and the BSF, at the rear side of the solar cell. Owing to the extremely close p^+ and n^+ regions, carriers can tunnel through the compensated polysilicon layer in between. The Figure 4.2 below shows the band diagrams of such IBC solar cell under different operating conditions.

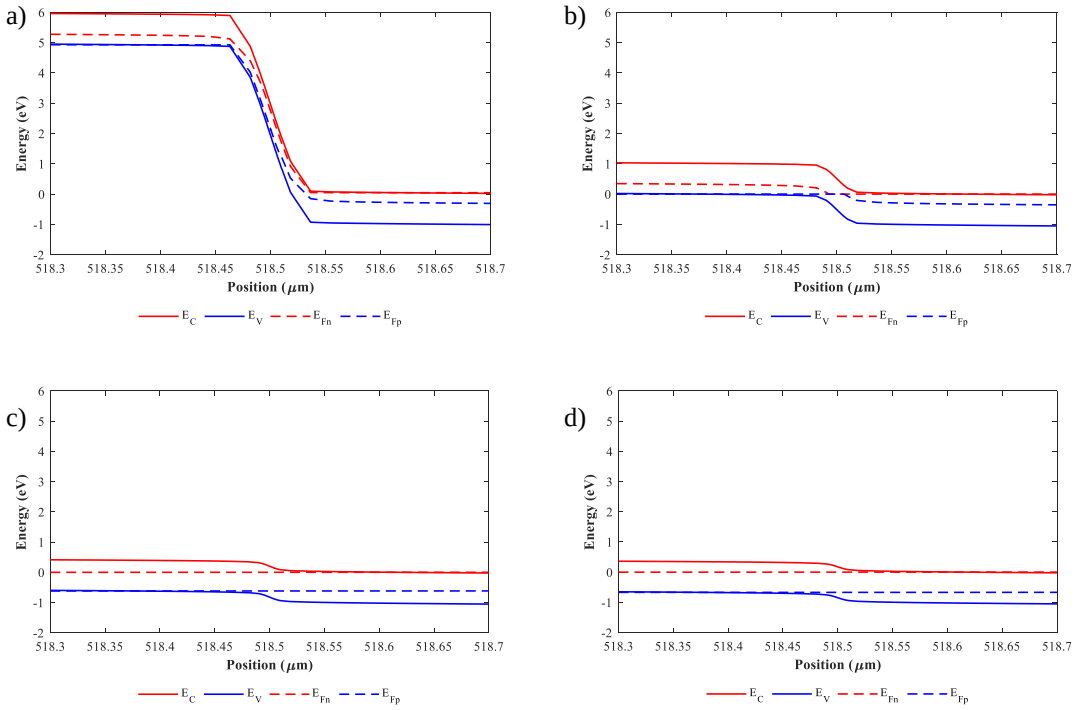

Figure 4.2: Band diagram of a) reverse bias −5 V; b) short circuit; c) maximum power point; d) open circuit conditions under 1000 $W m^{-2}$ illumination

Figure 4.2a illustrates the band diagram under a reverse bias of −5 V. The energy difference here of hole and electron quasi-Fermi levels, E_{Fp} and E_{Fn}, is slightly varying from the applied reverse voltage because the cutline is created horizontally. Hence, the band diagram here could only refer to the probability of tunneling through the gap region.

The quasi-Fermi level of the n^+ side conduction band is 0 all the time as shown in Figure 4.2. When the device is under reverse bias in Figure 4.2(a), the valence band of P side exceeds the conduction band of N side greatly, indicating the possibility of band-to-band tunneling through the gap region. Electrons accumulate at the bending point, tunneling through the narrow depletion region in between.

The band diagram at short circuit condition in Figure 4.2(b) shows a continuous quasi-Fermi level from P to N region. Both of the quasi-Fermi levels are zero in this situation and the valence band of P side. The edge of the valence band of P side keeps the same as that of N region, meaning the device is in equilibrium. The width of the depletion region is absolutely larger compared with the narrow path under reverse bias.

The p type quasi-Fermi levels of both regions are continuous when the device is under maximum power output and the open circuit conditions in Figure 4.2(c) and (d). Device under illumination reveals the potential of such solar cell. The difference of E_{Fp} and E_{Fn} is the largest when the device is under open circuit conditions.

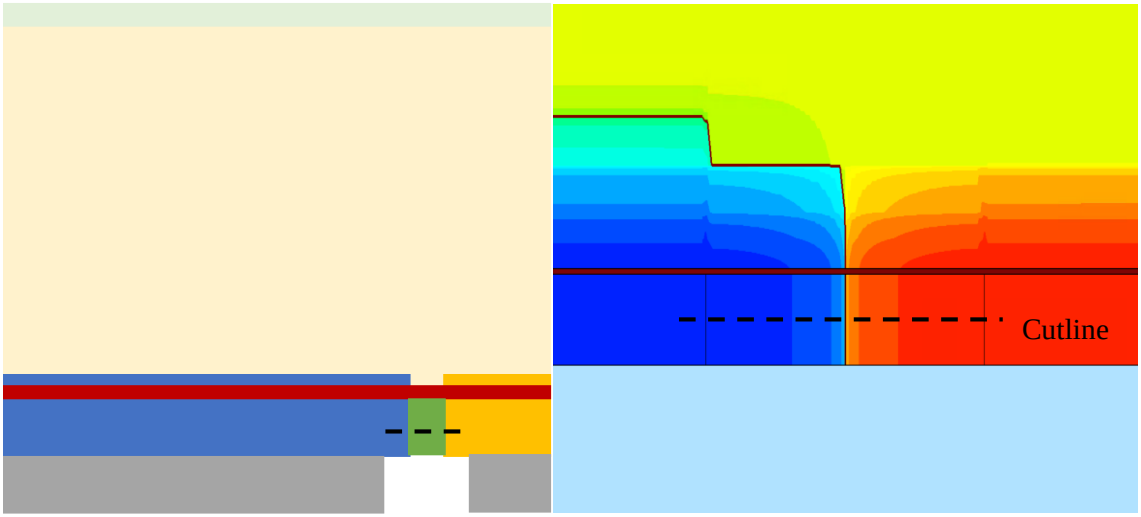

Figure 4.3: Cutline at the gap region of IBC solar cell

4.3. Effect of the tunneling mass

The analysis of cell structure and the band diagram under different operating points provides an insight of where the tunneling happens and how it occurs. The upcoming sections are going to analyze several important factors that affect the tunneling process.

Tunneling mass is a key parameter that influences the probability of tunneling. When the tunneling mass increases, the tunneling probability will decrease, which is explained in the previous chapter. Hence, the higher the value of tunneling mass is, the lower tunneling probability will be. The determination of the tunneling mass is done by experiments and has a reasonable range based on the materials, in other words, the tunneling mass is a fitting parameter. Figure 4.4 below provides an intuitive view of the reverse characteristics under different tunneling mass conditions.

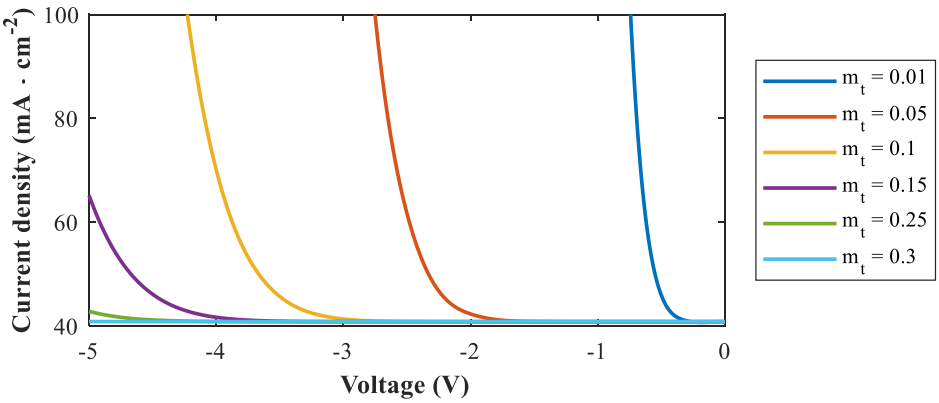

Figure 4.4: Reverse characteristics of different tunneling mass m_t

It is the high probability of tunneling through the gap region that reduces the breakdown voltage of such device. The reasonable range for polysilicon tunneling mass could be from 0.01 to 0.34 as illustrated in Figure 4.4. The tunneling mass of monocrystalline silicon is specified to 0.17. This is because monocrystalline silicon has a homogenous atomic structure where every atom follows and forms a single crystal. Polysilicon, on the other hand, consists of multiple small crystallites. The combination of such crystallites bring the grain boundaries that would act like defects in reality, hence, improving the probability of tunneling under reverse

bias compared with the monocrystalline silicon. Therefore, taking possible effects into account, the band-to-band tunneling mass of polysilicon is set to be 0.1 in the following analysis because band-to-band tunneling is the dominant mechanism in reverse bias of such highly doped device and is in favor of a low breakdown voltage. A previous study has proved that PV devices with low breakdown voltages have a higher annual energy yield than the conventional solar cells. Such advantage would not be obvious for breakdown voltages under −5 V [68]. Therefore, I-V characteristics of certain device only consider the breakdown voltage below −5 V.

4.4. Effect of the gap distance

The previous sections suggest that the most possible carrier transportation at the rear side of the IBC solar cells is band-to-band tunneling, which happens between those two carrier selective layers at the rear side of the solar cell and is fostered by a reasonable tunneling probability and a relatively small distance. In order to lower the essential voltage for conductivity under reverse bias, the simplest way is to narrow the width of the gap region. Figure 4.5 below presents the effect of gap distance on the reverse characteristics of the IBC solar cell when the dopant penetration length is fixed. Two different dopant diffusion lengths, 200 nm and 300 nm, are selected for three gap values.

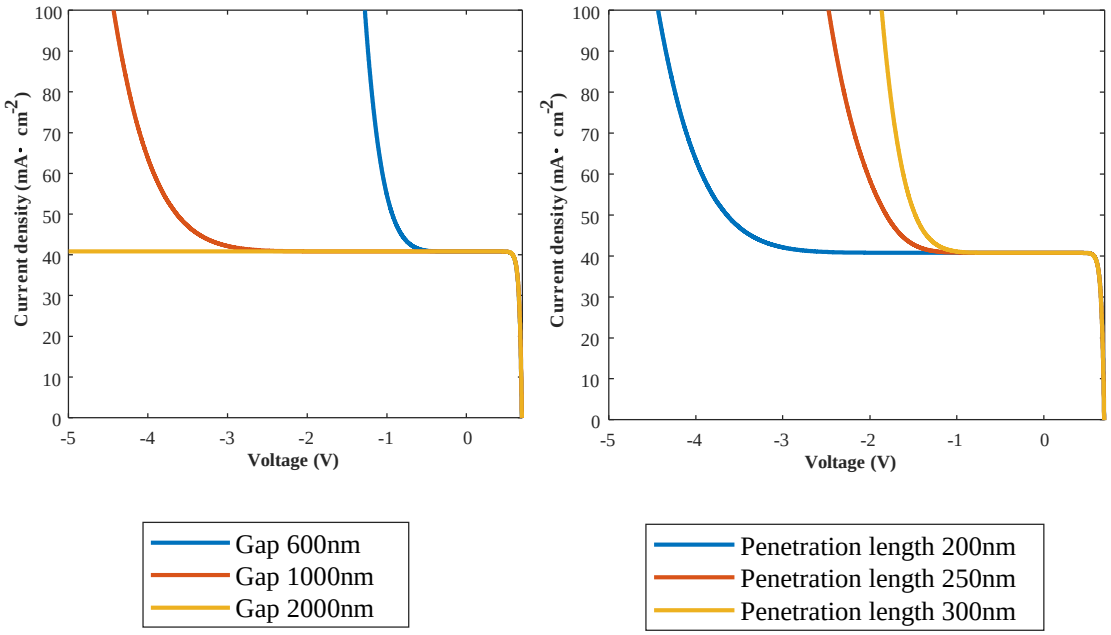

Figure 4.5: a) I-V characteristics of IBC cells for different gap widths for a dopant penetration length of 200 nm; b) I-V characteristics of IBC cells for different dopant penetration length for a gap width of 1 µm

With the decrease of the gap goes down the breakdown voltage of the IBC solar cell. The 600 nm gap manifests the earliest conductivity under reverse bias. The breakdown voltage goes down to −1.2 volt in this case. Reducing the penetration length has a similar effect to increase the gap width. Figure 4.1(b) indicates a smaller effective gap when the penetration length increases. Furthermore, an even lower breakdown voltage could be expected if the gap decreases further from the observations above.

It is incontrovertible that a smaller gap width will enhance the reverse characteristics but will also destroy the forward characteristics if it is too small. If the interval between the doped p^+ and n^+ regions at the rear side becomes too small, eventually, these two dopant diffusion regions inside the wafer will cause shunting due to the annealing process.

The fabrication process of IBC solar cells uses the lithography technology to grow the doped p^+ and n^+ regions at the rear side. The interval of these two regions are related to the size of the mask utilized in lithography as well. The laboratory standard for these masks could be in micrometer ranges while the industrial

caliber are mostly in hundreds micrometer. Giving considerations to both feasibility and practicality, the gap, which equals the interval of P and N regions, is set to be 1 µm.

4.5. Effect of the dopant diffusion length

Considering both the feasibility and the practicality, the interval of P and N regions is 1 µm. The effective distance, nevertheless, is still dependent on the dopant penetration length. The following subsections are going to analyze the effect of dopant penetration length from structural and electric perspectives.

4.5.1. Dopant concentration within the gap region

It has been explained that dopants are able to diffuse during the fabrication process of solar cells. High temperature annealing and the sputtering deposition contribute to the vertically diffusion process and the horizontally penetration. With the existence of silicon oxide layer, the diffusion depth into the wafer can be limited. However, the compensated polysilicon layer is in direct contact with two heavy doped P and N regions, consequently, penetration length over 160 nm will probably bring an engaged P and N regions within the gap. Figure 4.6 provides an illustration of two different penetration length and the corresponding rear side structures. The 230 nm penetration into the gap region eliminates the compensated region indicated in green which is visible in the 60 nm case.

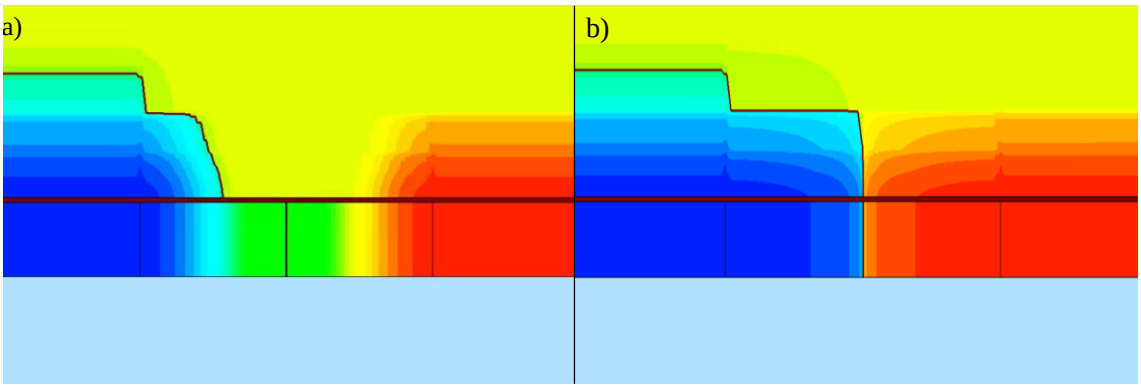

Figure 4.6: Different dopant penetration lengths. a) 60 nm penetration; b) 230 nm penetration

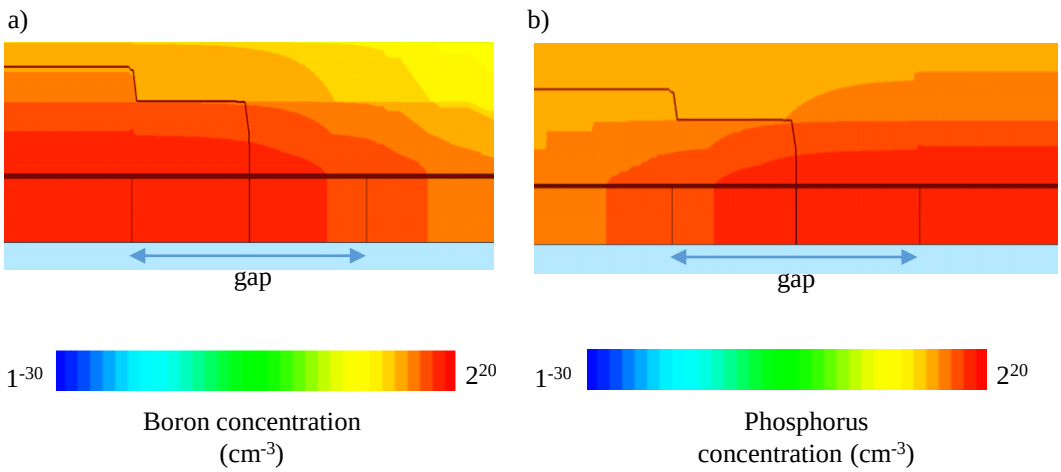

Figure 4.7: a) Boron concentration at P side; b) Phosphorus concentration at N side

Figure 4.7 further reveals such engagement. The boron and the phosphorus concentration at both sides have been illustrated. Both of the dopant penetration region have crossed the middle of the gap, reaching even the opposite layer. In consequence, all the gap region is no longer intrinsic but compensated. It is filled

with almost the same concentration level of two different dopant types. Although the Fermi level can still remain the middle of the bandgap. The material itself is no longer intrinsic.

4.5.2. Electric I-V characteristics

Figure 4.8 shows the external parameters and the breakdown voltage of the solar cell as a function of the dopant penetration length. The breakdown voltages of the IBC solar cell reach around −1 V when the penetration lengths of both p and n type dopants are more than 300 nm.

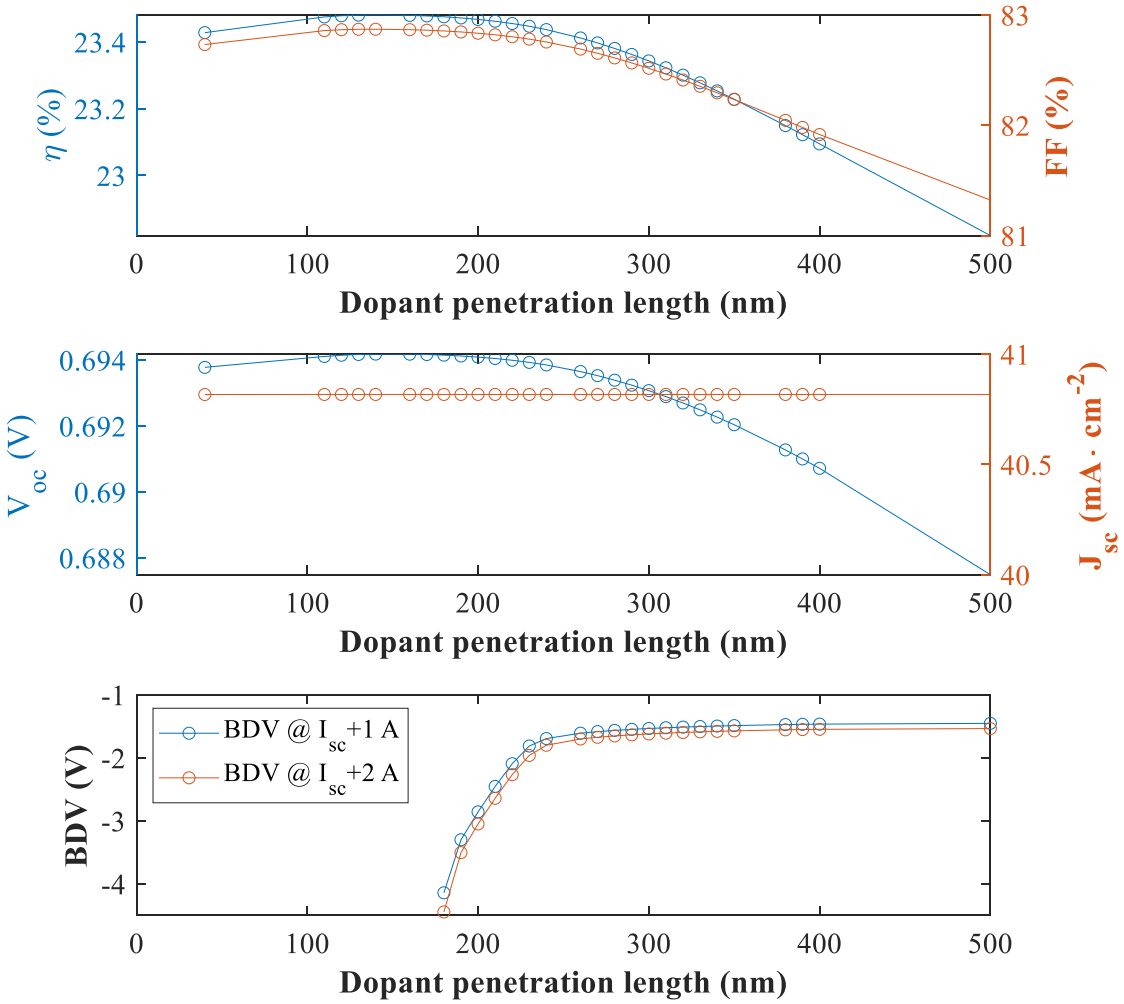

Figure 4.8: Reverse and forward characteristics of different penetration lengths

Figure 4.8 shows essential parameters, including efficiency, fill factor, open circuit voltage, short circuit current and breakdown voltage, for device performance evaluation. The efficiency and fill factor are in correspondence with the change of the open circuit voltage. The reason for the breakdown voltage to start at 5 V, as mentioned previously in this chapter, is that the range of breakdown voltage between −5 V and 0 V can imply an improvement in the annual energy yield [68]. Therefore, the reverse characteristics is only simulated within this voltage range that is of interest.

With the increasing penetration length comes the drop in open circuit voltage, which is due to the increase of recombination inside the crystalline silicon absorber. Fill factor decreases in correspondence with the open circuit voltage. The decrease of both the fill factor and the open circuit voltage contributes to a drop in cell efficiency consequently when the short circuit current remains almost the same.

However, the fill factor and the efficiency reaches the peak value when the penetration length is around 150 nm. Unlike the recombination process within the compensated polysilicon region, there can be two reasons for lower efficiency when the dopant penetration length decreases. The first one is a higher recombination on the interfaces of crystalline silicon based n type wafer and the silicon oxide layer [41]. The short penetration length leads to insufficient dopant concentration in the gap region, thus the recombination at the interface of wafer and silicon oxide layer can not be sufficiently suppressed.

Another reason for a lower efficiency when the dopant penetration length decreases is in the crystalline silicon wafer. For photogenerated electron and hole pairs above the gap region, the minority carriers must flow vertically and horizontally to be collected either by the p^+ emitter or the n^+ BSF at the rear side [39]. An insufficient carrier collection leads to a decrease of the efficiency of such device. When the penetration length is shorter, the horizontal distance for minority carriers become longer, thus, part of photogenerated electron and hole pairs recombine before being collected at he rear side.

The range of penetration length from 180 nm to 280 nm presents a rapid enhancement of breakdown voltages under reverse bias while the drop of efficiency is not evident. This range that fits the research goal of a low breakdown voltage while maintaining a favorable forward characteristic would probably be the next research stage for a reliable cell structure to maximize the annual energy yield.

4.6. Reflections

This chapter mainly reveals the influences of several structural parameters on the I-V characteristics of the device. With the reduction of gaps and penetration lengths goes down the breakdown voltage as they narrow the tunneling distance of carriers. The fitting parameter, tunneling mass, can vary from a wide range to indicate the probability of tunneling. A lower tunneling mass is in favor of a lower breakdown voltage. Cell performance under forward bias improves first due to the reduced recombination within the crystalline silicon wafer and on the interface between the silicon oxide layer and the crystalline silicon wafer. The device performance is deteriorated when penetration length continues to increase because of a higher recombination within the bulk when two dopant diffusion regions are closer. The breakdown voltage improves when the penetration length is longer.

5

Effect of working conditions parameters

In this chapter, the study of different working conditions and their influences on the reverse characteristics will be carried out. The chapter is divided into two parts, namely the irradiance simulations and temperature simulations.

5.1. Irradiance simulation

One of the crucial input in electric simulation of solar cell devices in Sentaurus TCAD is the optical generation profile. The profile indicates the number of photons absorbed per unit volume as a function of the position inside the solar cell.

5.1.1. Absorbed photon density

To calculate the optical absorption inside the device, the solar cell has been simulated using GenPro4 under AM1.5 spectrum [51].

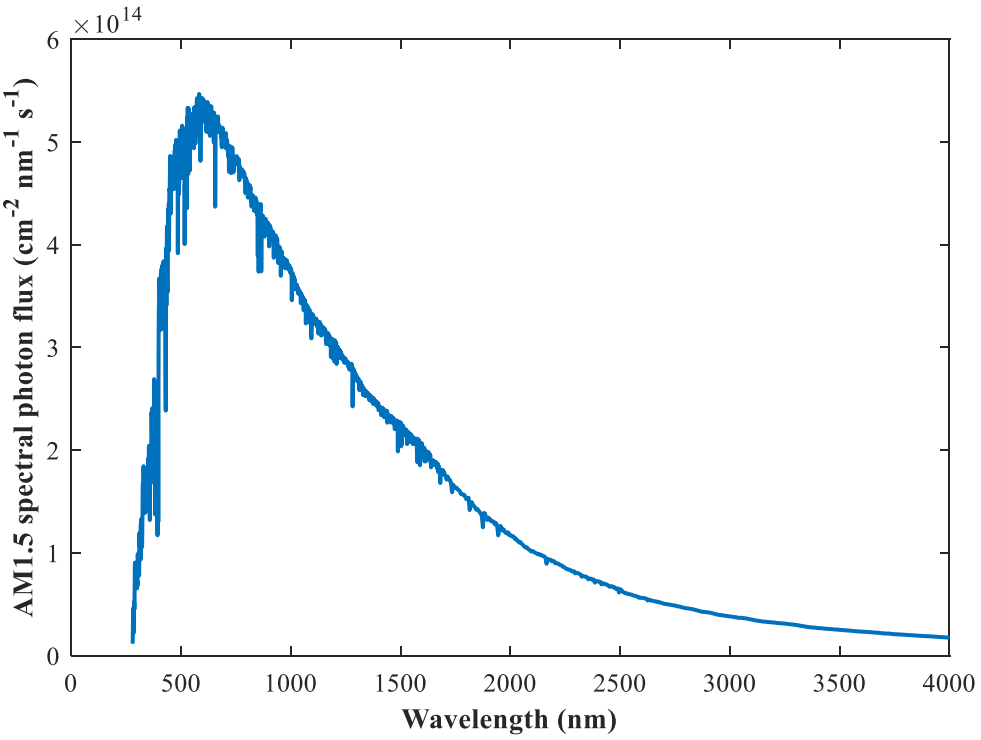

Figure 5.1: AM 1.5 spectrum

GenPro4 calculates the photon absorption at every position according to the device structural parameters, such as materials, layer thicknesses, the optical properties (n and k) and the solar spectrum. By assigning the amount of photons absorbed in each layer, Sentaurus simulations are accelerated because there is no need to recalculate the optical absorption profile in every simulation.

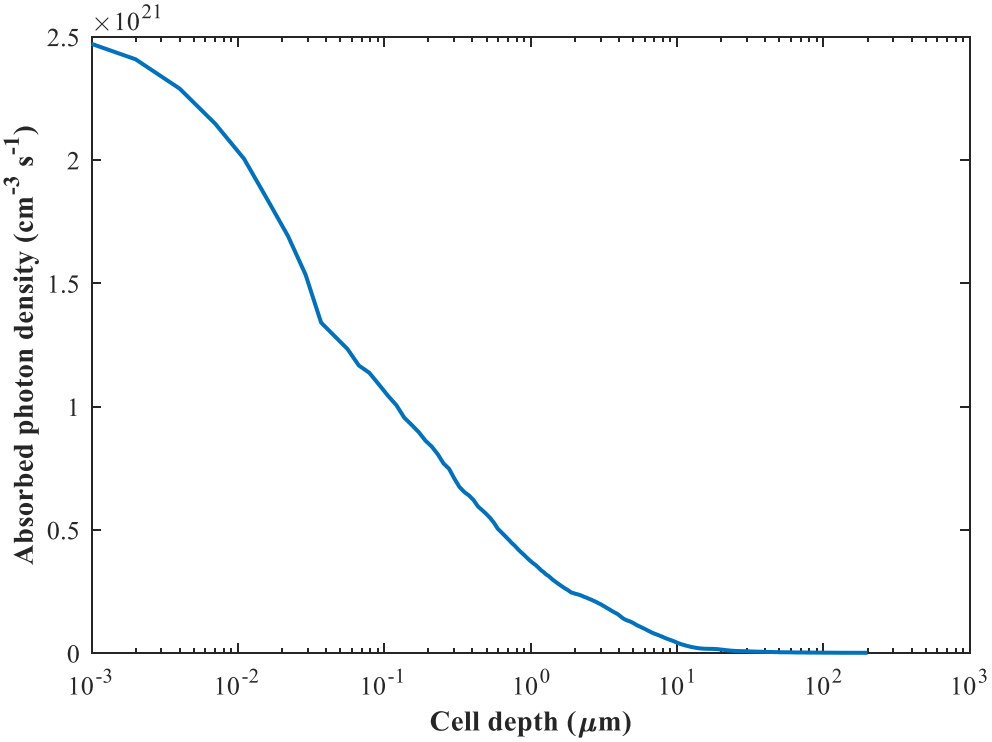

Figure 5.2: Photon absorption on every depth within the cell

Figures 5.1 and 5.2 show the incident spectral power density on the solar cell under AM1.5 spectrum and the simulation results of an textured surface IBC solar cell. The incident power density is 1000 $\mathrm{W\,m^{-2}}$ and the power density losses due to thermalization and below bandgap photons have been taken into account.

The optical analysis is essential when the device is under different illumination conditions. Ideally, a GenPro4 simulation should be carried out for every different illumination condition under which the I-V curve of the solar cell is evaluated. Nevertheless, an approximation is introduced to circumvent the complexity of this procedure. The optical profile for various irradiation conditions have been scaled proportionally to the total irradiance, and the absorption of photons at every depth uses the same proportion. For instance, when the incident power density is reduced to 500 $\mathrm{W\,m^{-2}}$, the photon absorption at every depth will then become half of that under 1000 $\mathrm{W\,m^{-2}}$ condition.

In addition, texturing on the surface has been removed as well for the purpose of accelerating the electrical simulation process. Since the value of absorbed photons is a function of the depth, the texturing on the cell surface is no longer necessary for the electric simulation. Besides, the mesh refinements on this texturing surface are complicated than the rest parts of the device. Hence, replacing the texturing surface with a flat anti-reflective coating simplifies the electric simulation without any interference with results.

5.1.2. Effect on the breakdown voltage

The previous section focuses on the optical generation profile in the simulation, the effect of different irradiation level will be analyzed in this section. In order to demonstrate the effects of irradiance and penetration length on the breakdown voltages, a contour plot containing both parameters is shown in Figure 5.3,

Various irradiation level have been selected from 0 $\mathrm{W\,m^{-2}}$ to 1000 $\mathrm{W\,m^{-2}}$. The range of the penetration lengths is from 200 nm to 400 nm. The color bar, from deep blue to light yellow, indicates the breakdown voltages from high to low. The x axis stands for the dopant diffusion lengths while y axis represents the incident power density. Figure 5.3 clearly shows an evenly distributed reverse characteristics along the y axis, meaning that irradiance has negligible effects on the breakdown voltages when the dopant penetration length is fixed.

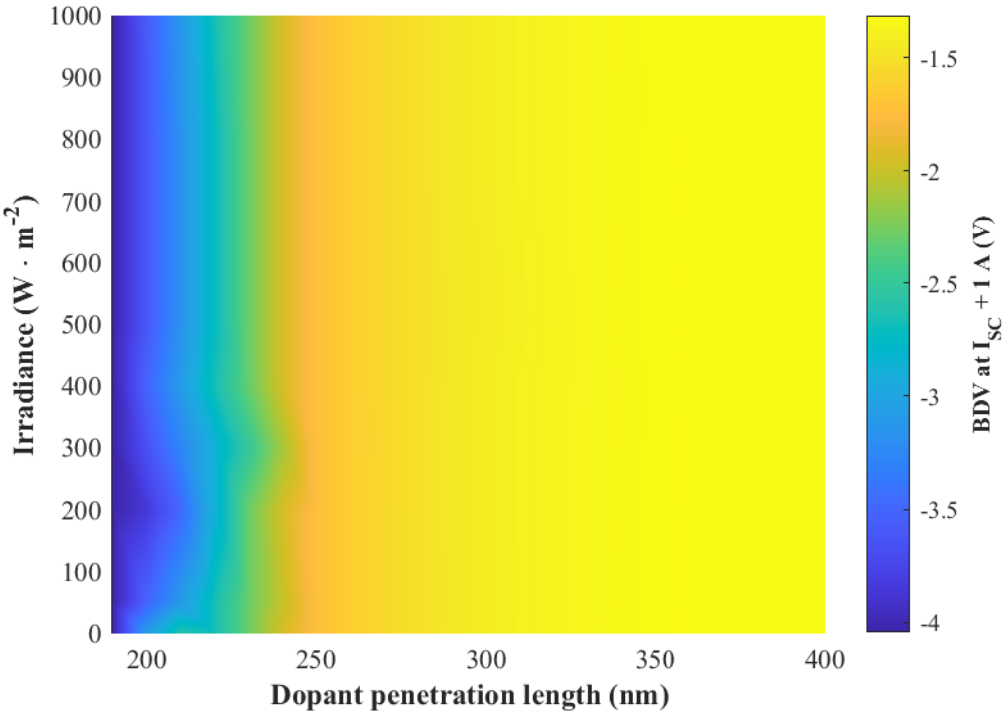

Figure 5.3: Breakdown voltages of various penetration lengths and irradiances

The penetration lengths remain the prime factor as for the enhancement of reverse characteristics. The simulation result along the X axis turns out that the breakdown voltages are dependent on the dopant penetration length especially in the range of 200 nm to 300 nm. The required conductive voltage decreases to −1.2 V from −4 V and keeps almost constant afterwards.

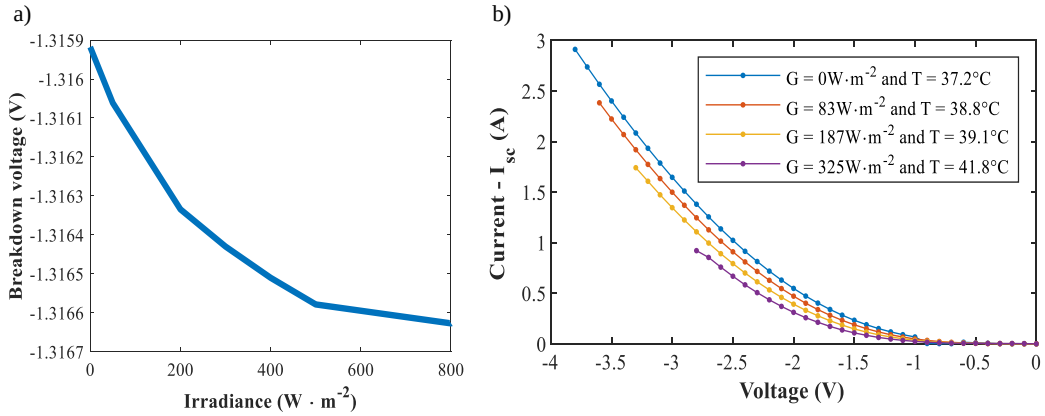

Figure 5.4: Effects of irradiance on breakdown voltages from a) simulation when the penetration length is 370 nm; b) experiment retrieved from [68]

The effect of irradiance is hardly visible in contour plot 5.3, thus, the breakdown voltages of different irradiation conditions at a fixed dopant penetration length 370 nm is illustrated in Figure 5.4(a) with the experimental measurements in Figure 5.4(b). The experimental measurements were taken on SunPower Gen3 IBC solar cells but the structure of such IBC is unknown. SunPower Gen3 IBC solar cells have a high open circuit voltage, hence, It is suspected that it is also an IBC solar cell with passivation contacts.

Normally, when a solar cell is under different illumination conditions, its forward characteristics change significantly. Both short circuit current and open circuit voltage will decrease when the irradiance decreases.

However, the reverse characteristics of certain device would mostly keep constant. Nevertheless, both of the figures convey the information of the positive correlation of irradiance and breakdown voltages. The breakdown voltages tend to decrease when the irradiance increases. Nevertheless, such reduction is not so obvious in simulations as in the experimental measurement. There is a large change in the breakdown voltage with irradiance in experiments. However, the simulation result does not show that. The differences of breakdown voltage in the simulation is only around 1 mV, which is relatively small.

One of the possible reasons for the different breakdown voltage changes are that both temperature and irradiance are included in comparisons. The changes in irradiance is sure to change the temperature of the device. As can be seen from Figure 5.4(b), device temperature are not exactly the same. Taking both temperature and irradiance into account, the breakdown voltage differences might be larger that that in simulations.

Another reason is regarding the cell structure. The measurement was carried out on SunPower Gen3 IBC solar cells. The structure of such IBC cell is unknown except both the simulated IBC cell and the SunPower Gen3 IBC cell have a high open circuit voltage. Different IBC cell structures are certain to bring simulation and experimental results.

5.2. Thermal simulations

Another crucial input in electrical simulation of solar cell devices in Sentaurus TCAD is the temperature. Temperature definitions include the lattice temperature and the electron and hole temperatures. The lattice temperature stands for the effects of total dissipated heat and is constant throughout the device [49].

5.2.1. Device temperature

The temperature in this project is only used as the device operating parameter, effects on absorbed charge carriers are not considered in this chapter. The temperature rise is mainly due to the self-heating by dissipating energy and is assumed to be uniform throughout the device.

Like all other semiconductor devices, solar cells are sensitive to temperature. Temperature modifies the shape of the I-V curve especially under forward bias. When the temperature rises, the bandgap of silicon decreases.

$$E_g(T) = E_g(0) - \frac{\alpha T^2}{T+\beta} \tag{5.1}$$

where $E_g(T)$, α and β are the fitting parameters. With the bandgap decreasing ,more photons would then be absorbed and collected, thus leading to a higher short circuit current [6].

Therefore, the inputs of GenPro4 have to be redefined every time the temperature changes. Since the rise of the temperature will lead to a decrease in bandgap of the device, the photon absorption of the device will increase correspondingly. However, the I-V curve is not very influential since it offsets the short circuit current for a preferable analysis of the reverse characteristics only.

5.2.2. Effect on the breakdown voltage

In order to demonstrate the effects of temperature and penetration length on the breakdown voltages, a contour plot containing both parameters is shown in Figure 5.5. Various temperature conditions have been selected from 0 °C to 70 °C. The range of the penetration lengths is from 220 nm to 400 nm. The reason for penetration length to start at 220 nm is all of simulations of penetration length below 220 nm fail. The color bar, from deep blue to light yellow, indicates the breakdown voltages from high to low. The x axis stands for the dopant penetration lengths and the y axis represents the incident power density. Figure 5.5 shows an evenly distributed reverse characteristics along the y axis as well. The penetration lengths are dominate compared with temperature as for the enhancement of reverse characteristics. The required conductive voltage decreases to 1.4 V from 2.7 V and keeps almost constant afterwards.

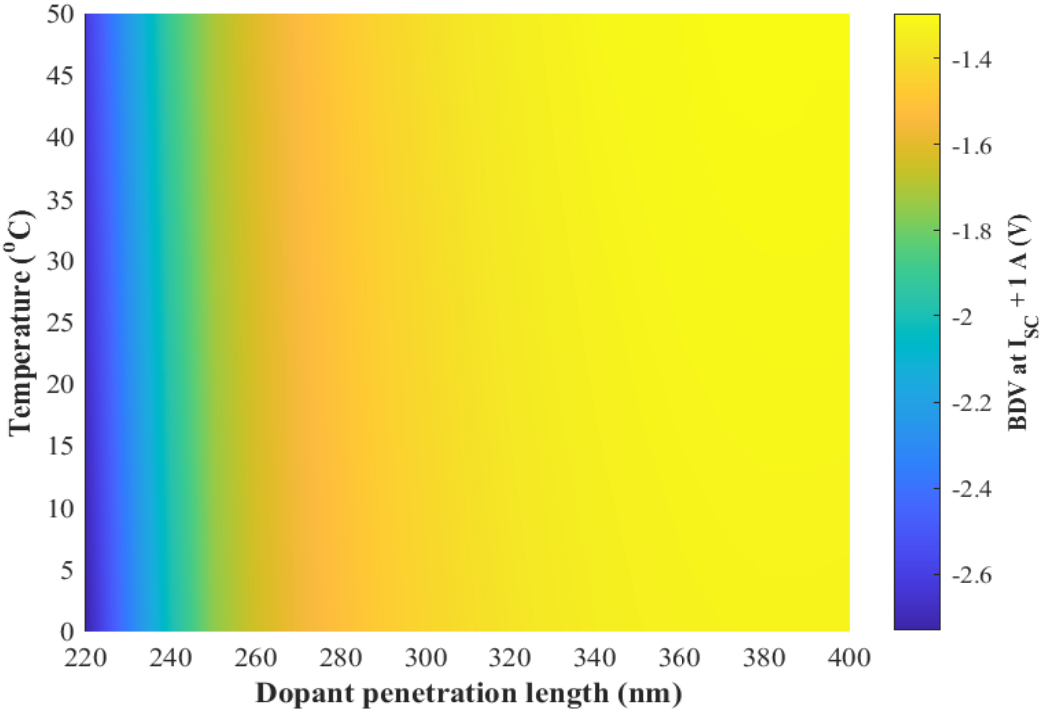

Figure 5.5: Breakdown voltages of various penetration lengths and temperatures

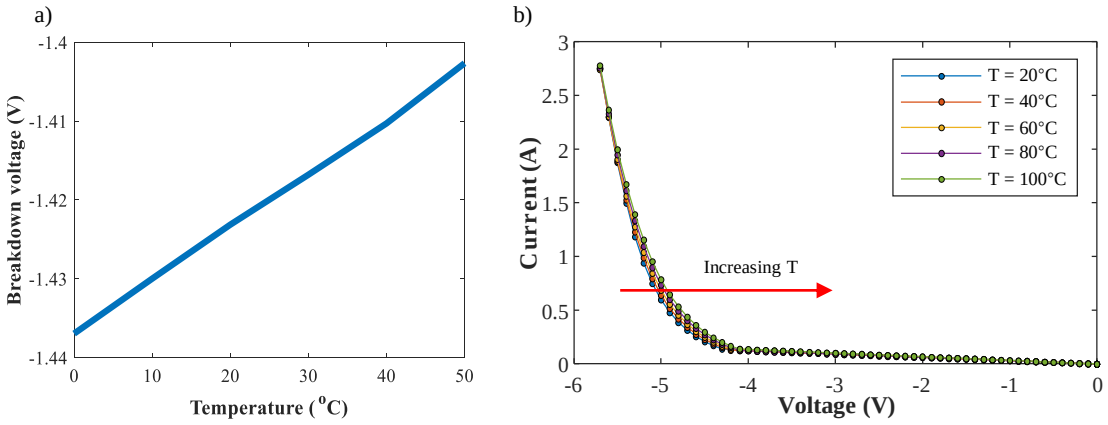

Figure 5.6: Effects of temperature on breakdown voltages from a) simulation when the penetration length is 370 nm; b) experiment retrived from [68]

The effect of irradiance is not obvious from Figure 5.5, thus, the breakdown voltages of different irradiation conditions at a fixed dopant penetration length 370 nm is illustrated in another figure 5.6a with the experimental measurements in figure 5.6b. Unlike the irradiance, both of the figures convey the information of the negative correlation of temperature and breakdown voltages. The possible reason can be that the temperature coefficient of tunneling is negative. For tunneling, which is among the Zener breakdown mechanisms, the electric field should be sufficiently high to torn electron from the valence band to the conduction band. Since the bandgap decreases when temperature increases, the electric field required to torn the valence electrons drops correspondingly. Consequently, the required voltage decreases because voltage equals the electric field intensity times the width of the space charge region, resulting in a negative temperature coefficient. Therefore, the higher the device temperature, the lower the breakdown voltage will be.

The possible reasons for the different breakdown voltage changes are similar to the previous analysis. Both temperature and irradiance are taken into account in the experiment but the simulation is carried out

based on temperature only. Another reason is regarding the cell structure. Different IBC cell structures are certain to bring simulation and experimental results.

5.3. Reflections

The optical simulation is done by GenPro4 to generate the photon absorption profile and Sentaurus does the electric simulation based on that profile. The results indicate that the breakdown voltage of the device increases with the increase of irradiance but the change of breakdown voltage is negligible. On the contrary, the increase in temperature lead to a decreasing breakdown voltage, which can be owing to the negative temperature coefficient of tunneling. However, penetration length is dominant to both irradiance and temperature in the influences on the breakdown voltage. The involvement of both temperature and irradiance in experiments can lead to differences in simulation and experimental results. Different cell structures can be possible reasons for such differences as well.

6

Conclusions and recommendations

The aim of this research was to identify the dominant mechanisms that determine the breakdown characteristics of interdigitated back contact solar cells and study the combined optimization of reverse and forward characteristics of interdigitated back contact solar cells.

6.1. Conclusions

This chapter summarizes the main the main research objectives proposed in the first chapter and the conclusions of this study.

1. *Investigate different solar cell structures that result in low breakdown characteristics and identify the charge carrier transport mechanisms involved under reverse bias conditions.*

   In front back contacted solar cells, the breakdown is mainly caused by avalanche effect. Charge carriers gain enough kinetic energy from the applied electric field to be separated from the covalent bonds. The free carriers, being accelerated, will further ionize the atoms on lattice. The process takes place within the entire bulk region. Hence, the breakdown voltages are usually below -10 V. In the case of front back contacted solar cells, the only possibility to improve the breakdown voltage is to create another path between the positive and negative contacts of the solar cell and this can be achieved with a integrated bypass diode.

   However, in IBC solar cells, the positive and negative contacts are much closer to each other and when the cell is reversed bias, the highly doped p^+ and n^+ regions allow carriers to recombine through band-to-band tunneling without entering the bulk of the solar cell. Band-to-band tunneling can happen where there is no gap between p^+ and n^+ regions in homojunction IBC cells or if the gap is filled with intrinsic polysilicon in heterojunction IBC cells.

2. *Generate a robust 2D simulation template to perform a parametric evaluation of the I-V characteristics of a solar cell.*

   Sentaurus TCAD was chosen to simulate the electrical performance of silicon heterojunction interdigitated back contact solar cells for its comprehensive functions. Initial conditions and material properties are assigned to every layer within the cell structure and meshes are generated as meticulous as needed to return a valid electrical output expeditiously.

3. *Analyze the influence of structural parameters and operating conditions on the forward and reverse I-V characteristics of a solar cell.*

   Widths of the gap region and lateral penetration lengths are the most important structural parameter that have an effect on the reverse I-V characteristics of the IBC-SHJ solar cells. A smaller gap and a longer penetration length contribute to reduce the width of the tunneling barrier, which leads to an increase in the tunneling current and an improvement of the cell's breakdown voltage. However, a smaller separation between the p^+ and n^+ regions in an IBC solar cell can lead to an increased recombination of the generated charge carriers inside the bulk of the solar cell as well. This can cause a deterioration of the forward characteristics, mainly the open circuit voltage and the efficiency of the solar cell.

Tunneling mass is a crucial fitting parameter to decide the probability of tunneling within a given material. A lower tunneling mass was in favor of a lower breakdown voltage and took consideration of other possible effects contributing to it.

Temperature and irradiance have limited influence on the reverse characteristics of IBC solar cells than on the forward characteristics. The changes in temperature and irradiance were negligible on device breakdown voltages compared to the effect of the penetration length. The sensitivity analysis of temperature and irradiance provides the base for further investigation into the energy yield of PV modules in realistic operating conditions.

6.2. Recommendations

This thesis project mainly focuses on the simulation of the breakdown characteristics of solar cells for shade tolerant PV modules. After the work carried out, several refinements and research lines are opened for further investigation.

First of all, the simplifications of temperature and irradiance could be refined. Scaling of irradiance cannot show the precise absorption of incident light within the device. The optical simulation can hardly reflect the incident light spectrum in reality. In addition, different temperatures are going to change the bandgap of materials, leading to a nonidentical photon absorption. It is expected that the results would show similar trends if accurate absorption profiles were generated when working conditions vary, and these results would make the research project more complete.

Secondly, a slightly different diffusion rate of boron and phosphorus in reality could be implemented to the simulation template. Such different diffusion rate of boron and phosphorus would result in a compensated polysilicon layer close to the n^+ region. The dopant diffusion regions inside the wafer would have different depths, and may lead to a higher degradation in forward characteristics.

Thirdly, the influences of irradiance and temperature on breakdown voltages could be extended. Temperature and irradiance can be interdependent, and the simulation results show the same trend but with negligible differences compared with that of experiments. In consequence, a comprehensive comparison of device performances under different working conditions could be carried out.

Finally, the simulated IBC solar cell achieved a low breakdown voltage while maintained a high efficiency within a certain penetration length. The designs would be more complete if the annual energy yield of such IBC solar cells could be estimated in system level simulation and measured in reality. Therefore, the fabrication process could be investigated to reveal the feasibility of commercializing these devices.

Bibliography

[1] Mário Brito and Tânia Sousaa. World primary energy production & consumption 1900-2010: What can be learned from past trends? *12th International Conference on Energy for a Clean Environment*, 2015.

[2] Vaclav Smil. *Energy: a beginner's guide*. Simon and Schuster, 2017.

[3] Antonio Zecca and Luca Chiari. Fossil-fuel constraints on global warming. *Energy Policy*, 38(1):1–3, 2010.

[4] Adrian E Raftery, Leontine Alkema, Patrick Gerland, Samuel J Clark, François Pelletier, Thomas Buettner, Gerhard Heilig, Nan Li, and Hana Sevcikova. White paper: Probabilistic projections of the total fertility rate for all countries for the 2010 world population prospects. In *United Nations expert group meeting on recent and future trends in fertility*, 2009.

[5] Paris Agreement. Paris agreement. In *Report of the Conference of the Parties to the United Nations Framework Convention on Climate Change (21st Session, 2015: Paris). Retrived December*, volume 4, page 2017. HeinOnline, 2015.

[6] Arno HM Smets, Klaus Jäger, Olindo Isabella, René ACMM Swaaij, and Miro Zeman. *Solar Energy: The physics and engineering of photovoltaic conversion, technologies and systems*. UIT Cambridge, 2015.

[7] Fredrick A Lindholm, Jerry G Fossum, and Edward L Burgess. Application of the superposition principle to solar-cell analysis. *IEEE transactions on electron devices*, 26(3):165–171, 1979.

[8] Kiran Ranabhat, Leev Patrikeev, Aleksandra Antal'evna-Revina, Kirill Andrianov, Valerii Lapshinsky, and Elena Sofronova. An introduction to solar cell technology. *Journal of Applied Engineering Science*, 14(4): 481–491, 2016.

[9] IEA. *Renewables 2020 Solar PV*. International Energy Agency, 2020.

[10] Kim Trapani and Miguel Redón Santafé. A review of floating photovoltaic installations: 2007–2013. *Progress in Photovoltaics: Research and Applications*, 23(4):524–532, 2015.

[11] H Scheer. Why eurosolar. *Sonnenenergie;(Germany, Federal Republic of)*, 13(6), 1988.

[12] Maria Carla Di Vincenzo, Dilay Kesten, and David Infield. Assessment of performance of building shading device with integrated photovoltaics in different urban scenarios. In *2010 IEEE International Conference on Sustainable Energy Technologies (ICSET)*, pages 1–5. IEEE, 2010.

[13] Suk Whan Ko, Young Chul Ju, Hye Mi Hwang, Jung Hun So, Young-Seok Jung, Hyung-Jun Song, Hee-eun Song, Soo-Hyun Kim, and Gi Hwan Kang. Electric and thermal characteristics of photovoltaic modules under partial shading and with a damaged bypass diode. *Energy*, 128:232–243, 2017.

[14] Mordechay Avrutsky. Systems and methods to provide enhanced diode bypass paths, April 26 2016. US Patent 9,324,885.

[15] Chandani Sharma and Anamika Jain. Solar panel mathematical modelling using simulink. *International Journal of Engineering Research and Applications*, 4(5):67–72, 2014.

[16] Boudewijn B Pannebakker, Arjen C de Waal, and Wilfried GJHM van Sark. Photovoltaics in the shade: one bypass diode per solar cell revisited. *Progress in photovoltaics: Research and Applications*, 25(10): 836–849, 2017.

[17] MA Green, E Gauja, and W Withayachamnankul. Silicon solar cells with integral bypass diodes. *Solar cells*, 3(3):233–244, 1981.

[18] Steve Albrecht and Bernd Rech. Perovskite solar cells: On top of commercial photovoltaics. *Nature Energy*, 2(1):1–2, 2017.

[19] JM Shannon. A majority-carrier camel diode. *Applied Physics Letters*, 35(1):63–65, 1979.

[20] Christiana Honsberg and Stuart Bowden. Pv education. *ORG.(access April-June 2013) http://pveducation. org/pvcdrom/properties-of-sunlight/sun-position-calculator*, 2014.

[21] Tom Markvart and Luis Castañer. Principles of solar cell operation. In *McEvoy's Handbook of Photovoltaics*, pages 3–28. Elsevier, 2018.

[22] Rudhard Klaus Müller. History of doping and doping control. *Doping in sports: Biochemical principles, effects and analysis*, pages 1–23, 2010.

[23] CA Mead and WG Spitzer. Fermi level position at metal-semiconductor interfaces. *Physical Review*, 134 (3A):A713, 1964.

[24] M Cid, N Stem, C Brunetti, AF Beloto, and CAS Ramos. Improvements in anti-reflection coatings for high-efficiency silicon solar cells. *Surface and Coatings Technology*, 106(2-3):117–120, 1998.

[25] Ronald Newburgh. Fresnel drag and the principle of relativity. *Isis*, 65(3):379–386, 1974.

[26] Jan Schmidt, Florian Werner, Boris Veith, Dimitri Zielke, S Steingrube, Pietro P Altermatt, Sebastian Gatz, Thorsten Dullweber, and Rolf Brendel. Advances in the surface passivation of silicon solar cells. *Energy Procedia*, 15:30–39, 2012.

[27] Ruy S Bonilla, Bram Hoex, Phillip Hamer, and Peter R Wilshaw. Dielectric surface passivation for silicon solar cells: A review. *physica status solidi (a)*, 214(7):1700293, 2017.

[28] Meng Tao, Darshak Udeshi, Nasir Basit, Eduardo Maldonado, and Wiley P Kirk. Removal of dangling bonds and surface states on silicon (001) with a monolayer of selenium. *Applied physics letters*, 82(10): 1559–1561, 2003.

[29] Soo Hyun Lee, Sang Hun Kim, and Jae Su Yu. Metal-semiconductor-metal near-ultraviolet (˜ 380 nm) photodetectors by selective area growth of zno nanorods and sio 2 passivation. *Nanoscale research letters*, 11(1):1–8, 2016.

[30] Alexandros Cruz, Er-Chien Wang, Anna B Morales-Vilches, Daniel Meza, Sebastian Neubert, Bernd Szyszka, Rutger Schlatmann, and Bernd Stannowski. Effect of front tco on the performance of rear-junction silicon heterojunction solar cells: Insights from simulations and experiments. *Solar Energy Materials and Solar Cells*, 195:339–345, 2019.

[31] A Schenk. Rigorous theory and simplified model of the band-to-band tunneling in silicon. *Solid-State Electronics*, 36(1):19–34, 1993.

[32] Yiming Liu, Yun Sun, and Angus Rockett. An improved algorithm for solving equations for intra-band tunneling current in heterojunction solar cells. *Thin Solid Films*, 520(15):4947–4950, 2012.

[33] J Wu, LF Register, and E Rosenbaum. Trap-assisted tunneling current through ultra-thin oxide. In *1999 IEEE International Reliability Physics Symposium Proceedings. 37th Annual (Cat. No. 99CH36296)*, pages 389–395. IEEE, 1999.

[34] Cassondra Neau and Kaushik Roy. Optimal body bias selection for leakage improvement and process compensation over different technology generations. In *Proceedings of the 2003 international symposium on Low power electronics and design*, pages 116–121, 2003.

[35] M Singh Tyagi. Zener and avalanche breakdown in silicon alloyed pn junctions—i: Analysis of reverse characteristics. *Solid-State Electronics*, 11(1):99–115, 1968.

[36] Dominik Lausch, Kai Petter, Bastian Henke, Ronny Bakowskie, Stefan Schweizer, and Christian Hagendorf. Classification of recombination active defect structures in multicrystalline silicon solar cells. *Energy Procedia*, 8:28–34, 2011.

[37] Thomas Lackner. Avalanche multiplication in semiconductors: A modification of chynoweth's law. *Solid-State Electronics*, 34(1):33–42, 1991.

[38] Michael D Lammert and Richard J Schwartz. The interdigitated back contact solar cell: A silicon solar cell for use in concentrated sunlight. *IEEE Transactions on Electron Devices*, 24(4):337–342, 1977.

[39] Haifeng Chu. *Interdigitated Back Contact Silicon Solar Cells: Metallization and Reverse Bias Characteristics*. PhD thesis, University of Konstanz, 2019.

[40] Jimmy Melskens, Bas WH van de Loo, Bart Macco, Lachlan E Black, Sjoerd Smit, and WMM Kessels. Passivating contacts for crystalline silicon solar cells: From concepts and materials to prospects. *IEEE Journal of Photovoltaics*, 8(2):373–388, 2018.

[41] C Hollemann, F Haase, M Rienäcker, V Barnscheidt, J Krügener, N Folchert, R Brendel, S Richter, S Großer, E Sauter, et al. Separating the two polarities of the polo contacts of an 26.1%-efficient ibc solar cell. *Scientific reports*, 10(1):1–15, 2020.

[42] Ujjwal Das, Jianbo He, Zhan Shu, Lulu Zhang, Chris Thompson, Robert Birkmire, and Steven Hegedus. Sensitivity of surface passivation and interface quality in ibc-shj solar cells to patterning process. In *2013 IEEE 39th Photovoltaic Specialists Conference (PVSC)*, pages 1224–1227. IEEE, 2013.

[43] Paul Procel, Guangtao Yang, Olindo Isabella, and Miro Zeman. Numerical simulations of ibc solar cells based on poly-si carrier-selective passivating contacts. *IEEE Journal of Photovoltaics*, 9(2):374–384, 2019.

[44] Haifeng Chu, Lejo J Koduvelikulathu, Valentin D Mihailetchi, Giuseppe Galbiati, Andreas Halm, and Radovan Kopecek. Soft breakdown behavior of interdigitated-back-contact silicon solar cells. *Energy Procedia*, 77:29–35, 2015.

[45] David D Smith, Peter J Cousins, Asnat Masad, Ann Waldhauer, Staffan Westerberg, Michael Johnson, Xiuwen Tu, Tim Dennis, Gabriel Harley, Genevieve Solomon, et al. Generation iii high efficiency lower cost technology: Transition to full scale manufacturing. In *2012 38th IEEE Photovoltaic Specialists Conference*, pages 001594–001597. IEEE, 2012.

[46] Ralph Müller, Christian Reichel, Julian Schrof, Milan Padilla, Marisa Selinger, Ino Geisemeyer, Jan Benick, and Martin Hermle. Analysis of n-type ibc solar cells with diffused boron emitter locally blocked by implanted phosphorus. *Solar Energy Materials and Solar Cells*, 142:54–59, 2015.

[47] Otwin Breitenstein, Jan Bauer, Karsten Bothe, Wolfram Kwapil, Dominik Lausch, Uwe Rau, Jan Schmidt, Matthias Schneemann, Martin C Schubert, Jan-Martin Wagner, et al. Understanding junction breakdown in multicrystalline solar cells. *Journal of Applied Physics*, 109(7):5, 2011.

[48] Feng Li, Dawei Liu, Ziqian Wang, Jinye Zhai, Wei Zhang, Yanjiao Shen, Jinchao Shi, Dengyuan Song, Ilkay Cesar, Nicolas Guillevin, et al. Development of large-area bifacial interdigitated-back-contact (ibc) solar cell with industrial production environment. In *2018 IEEE 7th World Conference on Photovoltaic Energy Conversion (WCPEC)(A Joint Conference of 45th IEEE PVSC, 28th PVSEC & 34th EU PVSEC)*, pages 3722–3726. IEEE, 2018.

[49] TCAD Synopsys. Sdevice manual. *Release H-2013.03, Zurich, Switzerland*, 2008.

[50] Sentaurus User Guide and L Version. Synopsys tcad sentaurus. *San Jose, CA, USA*, 2016.

[51] Rudi Santbergen, Tomomi Meguro, Takashi Suezaki, Gensuke Koizumi, Kenji Yamamoto, and Miro Zeman. Genpro4 optical model for solar cell simulation and its application to multijunction solar cells. *IEEE journal of photovoltaics*, 7(3):919–926, 2017.

[52] Hugh E DeWitt. Evaluation of the quantum-mechanical ring sum with boltzmann statistics. *Journal of Mathematical Physics*, 3(6):1216–1228, 1962.

[53] OW Greenberg. Particles with small violations of fermi or bose statistics. *Physical Review D*, 43(12):4111, 1991.

[54] Robert K Niven. Exact maxwell–boltzmann, bose–einstein and fermi–dirac statistics. *Physics Letters A*, 342(4):286–293, 2005.

[55] Takashi Fuyuki and Hiroyuki Matsunami. Electronic properties of the interface between si and tio2 deposited at very low temperatures. *Japanese Journal of Applied Physics*, 25(9R):1288, 1986.

[56] Gerhard K Wachutka. Rigorous thermodynamic treatment of heat generation and conduction in semiconductor device modeling. *IEEE transactions on computer-aided design of integrated circuits and systems*, 9(11):1141–1149, 1990.

[57] A Schenk and S Müller. Analytical model of the metal-semiconductor contact for device simulation. In *Simulation of Semiconductor Devices and Processes*, pages 441–444. Springer, 1993.

[58] K Varahramyan and EJ Verret. A model for specific contact resistance applicable for titanium silicide-silicon contacts. *Solid-State Electronics*, 39(11):1601–1607, 1996.

[59] Hiroyoshi Tanimoto, Masaki Kondo, Toshiyuki Enda, Nobutoshi Aoki, Ryosuke Iijima, Takeshi Watanabe, Mariko Takayanagi, and Hidemi Ishiuchi. Modeling of electron mobility degradation for hfsion misfets. In *2006 International Conference on Simulation of Semiconductor Processes and Devices*, pages 47–50. IEEE, 2006.

[60] DBM Klaassen. A unified mobility model for device simulation—i. model equations and concentration dependence. *Solid-State Electronics*, 35(7):953–959, 1992.

[61] C Canali, G Majni, R Minder, and G Ottaviani. Electron and hole drift velocity measurements in silicon and their empirical relation to electric field and temperature. *IEEE Transactions on electron devices*, 22 (11):1045–1047, 1975.

[62] W Bludau, A Onton, and W Heinke. Temperature dependence of the band gap of silicon. *Journal of Applied Physics*, 45(4):1846–1848, 1974.

[63] Herbert S Bennett and Charles L Wilson. Statistical comparisons of data on band-gap narrowing in heavily doped silicon: Electrical and optical measurements. *Journal of applied physics*, 55(10):3582–3587, 1984.

[64] Changiz Vatankhah and Ali Ebadi. Quantum size effects on effective mass and band gap of semiconductor quantum dots. *Research Journal of Recent Sciences*, 2277:2502, 2013.

[65] JG Fossum, RP Mertens, DS Lee, and JF Nijs. Carrier recombination and lifetime in highly doped silicon. *Solid-state electronics*, 26(6):569–576, 1983.

[66] RR King, RA Sinton, and RM Swanson. Studies of diffused phosphorus emitters: saturation current, surface recombination velocity, and quantum efficiency. *IEEE Transactions on electron devices*, 37(2): 365–371, 1990.

[67] W Lochmann and A Haug. Phonon-assisted auger recombination in si with direct calculation of the overlap integrals. *Solid State Communications*, 35(7):553–556, 1980.

[68] Andres Calcabrini, Viswambher Kambhampati, Patrizio Manganiello, Miro Zeman, and Olindo Isabella. A simulation study of reconfigurable modules for higher yields in partially shaded pv systems. In *2021 48th IEEE Photovoltaic Specialists Conference (PVSC)*. IEEE, 2021.